
TIBBİ ULTRASONOGRAFİ DERNEĞİ
The Society of Medical Ultrasonography
İZMİR - 1985
EUROSON SCHOOL
EUROSON SCHOOL 2026
CURRENT CONCEPTS IN
DIAGNOSTIC AND INTERVENTIONAL
ULTRASOUND
Istanbul
3-4 OCTOBER 2026
POINT BARBAROS ISTANBUL HOTEL
www.ultrasoundist.com.tr

EUROSON SCHOOL 2026

REGISTRATION & ACCOMMODATION

INVITATION

Dear Colleagues,

The Society of Medical Ultrasonography - TÜRKİYE is honored to invite you to the EUROSON SCHOOL of "Current Concepts in Diagnostic and Interventional Ultrasound" which will be held in Istanbul on 3 to 4 October 2026.

The meeting is planned to cover the theoretical and practical aspects of current ultrasound techniques and technologies with the contribution of experts. Attendees of hands-on sessions will find one-on-one time practice opportunity together with the skilled hands working on specific techniques.

Abstracts will be accepted for scientific oral and poster presentations in the field of ultrasound. We are looking forward to your participation.

Sincerely,

Prof. Dr. Suna ÖZHAN OKTAR
President The Society of
Medical Ultrasonography
Türkiye

EUROSON SCHOOL 2026

REGISTRATION & ACCOMMODATION

SCIENTIFIC COMMITTEES

Scientific Program Co-Chairs

Suna OZHAN OKTAR
Mustafa SECIL

Co-General Secretaries

Mahi Nur CERIT
Halit Nahit ŞENDUR

Organization Comittee

S. Sureyya OZBEK
Alper OZEL
Artur SALMASLIOGLU
Adnan KABAALIOGLU
Esra OZKAVUKCU
Hakan OZGUL
Mahi Nur CERIT
Halit Nahit SENDUR

Faculty

Richard BARR
Vito CANTISANI
Giovanna FERRAIOLI
Paul SIDHU
Maija RADZANI
Michele BERTOLOTTO
Suha Sureyya OZBEK
Mustafa SECIL
Suna Ozhan OKTAR
Alper OZEL
Artur SALMASLIOGLU
Serkan ARIBAL
Halit Nahit SENDUR
Mahi Nur CERIT
Levent OGUZKURT
Serap GULTEKIN
Baris BAKIR
Ali BALCI

EUROSON SCHOOL 2026

SCIENTIFIC PROGRAM

03 OCTOBER 2026	HALL 1	03 OCTOBER 2026	HALL 2
08.30-08.40	**Opening, Introduction**		
Chair:	Suna Ozhan Oktar, Mustafa Secil		
08.40-10.10	**Emerging Technologies in Ultrasound: Innovations and Future Direction** Technology presentations of vendors		
10.10-10.30	**Ultrasound Elastography: Update** Richard G. Barr		
10.30-11.00	**COFFEE BREAK**	**10.30-11.00**	**COFFEE BREAK**
11.00-12.30	**Liver Ultrasound - Elastography and Fat Quantification Techniques**	11.00-12.30	**Oral Presentations**
Chair:	Paul S. Sidhu		
11.00-11.20	**Liver Elastography Technique, Applications** Richard G. Barr		
11.20-11.40	**Liver Elastography Guidelines-Update** Giovanna Ferraioli		
11.40-12.00	**US-Based Hepatic Fat Quantification Techniques** Giovanna Ferraioli		
12.00-12.20	**Contrast-Enhanced Ultrasound of the Liver** Paul S. Sidhu		
12:20-12:30	**DISCUSSION**		
12.30-13.30	**LUNCH**	**12.30-13.30**	**LUNCH**
13.30-15.00	**Thyroid Ultrasound - Current Techniques and Interventions**	13.30-15.00	**Genitourinary US - Current Techniques and Interventions**
Chair:	S. Sureyya Ozbek	Chair:	Alper Ozel
13.30-13.50	**Evaluation of Thyroid Nodules: TI-RADS and Other Classifications** Artur Salmasliogl	13.30-13.50	**Testis Multiparametric Ultrasound Update 2026** Michele Bertolott
13.50-14.10	**Multiparametric Ultrasound of Thyroid** Mustafa Secilu	13.50-14.10	**Penile Ultrasound** Michele Bertolottoo
14.10-14.30	**Thyroid Pathologies Other Than Nodular Diseases** Suhha Sureyya Ozbek	14.10-14.30	**Benign Disorders of the Prostate** Artur Salmaslioglu
14.30-14:50	**Ablation of Thyroid Nodules and Parathyroid Lesions** Halit Nahit Sendur	14.30-14:50	**US Guided Focal Treatments and Fusion Biopsy of Prostate** Baris Bakir
14:50-15:00	**DISCUSSION**	14:50-15:00	**DISCUSSION**
10.30-11.00	**COFFEE BREAK**	**10.30-11.00**	**COFFEE BREAK**
15.30-17:30	**HANDS-ON** Liver, Thyroid	**15.30-17:30**	**HANDS-ON** Liver, Thyroid

EUROSON SCHOOL 2026

SCIENTIFIC PROGRAM

04 OCTOBER 2026 — HALL 1

08.30-10.00	**Breast US - Current Techniques and Interventions**
Chair:	Serap Gultekin
08.30-08.50	**Lesion Characterization**
	Serap Gultekin
08.50-09.10	**Elastography and CEUS in Breast**
	Richard G. Barr
09.10-09:30	**Biopsy and Fusion Biopsy of Breast Lesions**
	Serap Gultekin
09.30-09:50	**US Guided Ablation Treatments in Breast**
	Serkan Aribal
09:50-10:00	**DISCUSSION**
10.00-10.30	**COFFEE BREAK**
10.30-12.00	**Artificial Intelligence in Ultrasound**
Chair:	Suha Sureyya Ozbek
10.30-10.50	**AI for Detection of Thyroid and Breast Nodules**
	Vito Cantisani
10.50-11.10	**Future Perspectives in Mutiparametric US and AI**
	Maija Radzina
11.10-11.30	**AI to Quantify Fat**
	Giovanna Ferraioli
11.30-11.50	**AI - Friend and Foe of the Journal Editor**
	Paul Sidhu
11:50-12:00	**DISCUSSION**
12.00-13.30	**LUNCH**
13.30-15.00	**Interventional Techniques Current Trends**
Chair:	Adnan Kabaalioglu
13.30-13.50	**Evolution of Vascular Access in Interventional Radiology**
	Levent Oguzkurt
13.50-14.10	**US Guided Liver Biposy and Ablation**
	Halit Nahit Sendur
14.10-14.30	**Uterine Myoma Ablation with Sonographic Guidance**
	Serkan Aribal
14.30-14:50	**Renal Biopsy and Tumor Ablation**
	Mahi Nur Cerit
14:50-15:00	**DISCUSSION**
15.00-15.30	**COFFEE BREAK**
15.30-17.30	**HANDS-ON** Biopsy and Ablation Techniques Hands-On Varicose vein evaluation Hands-on

04 OCTOBER 2026 — HALL 2

08.30-10.00	**Vascular US - Current Techniques and Interventions**
Chair:	Artur Salmaslioglu
08.30-08.50	**Vascular CEUS: When and Why: A 2026 Update**
	Vito Cantisani
08.50-09.10	**Recent Advances in Vascular Ultrasound Imaging**
	Suna Ozhan Oktar
09.10-09:30	**Carotid Plaque Imaging**
	Maija Radzina
09.30-09:50	**Varicose Veins: Evaluation and Endovenous Treatment**
	Levent Oguzkurt
09:50-10:00	**DISCUSSION**
10.00-10.30	**COFFEE BREAK**
10.30-12.00	**Neck - Current Techniques and Interventions**
Chair:	Elshad Sadigov
10.30-10.50	**Ultrasound of Salivary Glands**
	Mustafa Secil
10.50-11.10	**Parathyroid Lesions**
	Alper Ozel
11.10-11.30	**Current Concepts Lymph Node Imaging**
	Mahi Nur Cerit
11.30-11.50	**Biopsy of Thyroid Nodules and Lymph Nodes**
	Suna Ozhan Oktar
11:50-12:00	**DISCUSSION**
12.00-13.30	**LUNCH**
13.30-15.00	**Musculoskeletal US Current Techniques**
Chair:	Ali Balci
13.30-14.00	**Musculoskeletal US Techniques**
	Ali Balci
14.00-14.30	**Musculoskeletal Sonoelastography**
	Ali Balci
14.30-14.50	**US in Peripheral Nerve Pathology**
	Maija Radzina
14:50-15:00	**DISCUSSION**
15.00-15.30	**COFFEE BREAK**
15.30-17.30	**HANDS-ON** Biopsy and Ablation Techniques Hands-On Varicose vein evaluation Hands-on

Oral Presentations

S-01

Quantitative Ultrasound and Metabolic Insulin Resistance in Hepatic Steatosis: Do TAI and TSI Reflect METS-IR?

Fatma Öztora, Halis Harun Öztürk, Atakan Küskün, Muzaffer Savaş Tepe

Kırklareli University Medical School, Department of Radiology, Kırklareli, Türkiye

AIM

Quantitative ultrasound (QUS) enables objective assessment of hepatic steatosis through tissue attenuation and scattering characteristics. Metabolic Score for Insulin Resistance (METS-IR) is a non-insulin-based surrogate marker of insulin resistance. This study aimed to investigate the relationships of QUS-derived tissue attenuation imaging (TAI) and tissue scatter-distribution imaging (TSI) with METS-IR in patients with hepatic steatosis and to evaluate their ability to discriminate elevated METS-IR.

METHODS

This retrospective study included adults with sonographically detected hepatic steatosis who had available QUS measurements and sufficient clinical and laboratory data for METS-IR calculation. METS-IR was calculated from body mass index, fasting glucose, triglycerides, and high-density lipoprotein cholesterol. Associations of METS-IR with TAI and TSI were evaluated using Spearman's rank correlation. Receiver operating characteristic (ROC) analysis was performed to assess the ability of TAI and TSI to discriminate elevated METS-IR, defined as METS-IR >=42.2 based on a previously reported cutoff for insulin resistance in a Turkish population. The optimal TSI cutoff was determined using the Youden index.

RESULTS

The study population comprised 88 patients (62 women, 70.5%; mean age, 52.0±14.0 years). METS-IR showed a moderate positive correlation with TSI (ρ=0.534, $p<0.001$), whereas its correlation with TAI was weak and non-significant (ρ=0.207, $p=0.053$). TSI discriminated elevated METS-IR with an area under the ROC curve (AUC) of 0.766 (95% CI, 0.664-0.868; $p<0.001$). A TSI cutoff of 95.25 provided 59.6% sensitivity and 83.9% specificity. In contrast, TAI showed no significant discriminative ability (AUC=0.546; 95% CI, 0.426-0.666; $p=0.451$).

CONCLUSION

TSI, but not TAI, was associated with METS-IR and showed significant ability to discriminate elevated METS-IR in patients with hepatic steatosis. These findings suggest that QUS-derived tissue scattering characteristics may reflect metabolic alterations associated with insulin resistance and could provide complementary information in the quantitative evaluation of hepatic steatosis.

KEYWORDS

Quantitative ultrasound, Hepatic steatosis, METS-IR, Insulin resistance, Tissue scatter distribution imaging

S-03

B-Mode Ultrasonography, Strain Elastography, and Doppler Assessment in de Quervain Tenosynovitis: A Cross-Sectional Study Correlated With Clinical Pain Scores

Mehmet Kutlu[1], Mehmet Numan Çolakoğlu[2], Erdem Özkan[3], Mehtap Balaban[4]

[1] Ankara Bilkent City Hospital, Department of Radiology, Ankara, Turkey

[2] Near East University Faculty of Medicine, Department of Radiology, Nicosia, Cyprus

[3] Kastamonu Training and Research Hospital, Department of Radiology, Kastamonu, Turkey

[4] Ankara Yıldırım Beyazıt University Faculty of Medicine, Department of Radiology, Ankara, Turkey

AIM

The clinical diagnosis of de Quervain tenosynovitis (DQT) relies on subjective provocative tests such as the Eichhoff and Finkelstein maneuvers, increasing the need for objective imaging criteria. We aimed to evaluate the diagnostic performance of B-mode ultrasonography, strain elastography, and Power Doppler in DQT, to assess the relationship between sonographic findings and the Visual Analog Scale (VAS), and to develop a new radiologic diagnostic score (DQRTS) combining these parameters.

METHODS

In this single-center, prospective, case-control diagnostic accuracy study, 50 DQT patients with positive Eichhoff/Finkelstein tests and 50 age- and sex-matched healthy controls were included. Abductor pollicis longus (APL) and extensor pollicis brevis (EPB) tendon thickness, extensor retinaculum thickness, peritendinous fluid, Power Doppler vascularity, and strain elastography patterns were assessed by two blinded radiologists. Diagnostic performance was evaluated by ROC analysis, and inter-observer agreement by intraclass correlation coefficient (ICC) and quadratic-weighted Kappa. DQRTS was designed and validated using Random Forest Gini importance scores with 10-fold cross-validation and LOOCV.

RESULTS

All B-mode measurements were significantly higher in patients than controls ($p<0.001$). Extensor retinaculum thickness showed the highest performance at >=0.70 mm (AUC=0.985, sensitivity 94%, specificity 94%), followed by APL thickness >=3.50 mm (AUC=0.963) and EPB thickness >=2.30 mm (AUC=0.832). After Bonferroni correction, the VAS-Finkelstein score correlated positively with EPB thickness ($\rho=0.432$) and negatively with APL strain score ($\rho=-0.426$). Inter-observer agreement was near-perfect (ICC=0.930-0.941). At >=12 points, DQRTS yielded 97% accuracy (sensitivity 96%, specificity 98%, AUC=0.992).

CONCLUSION

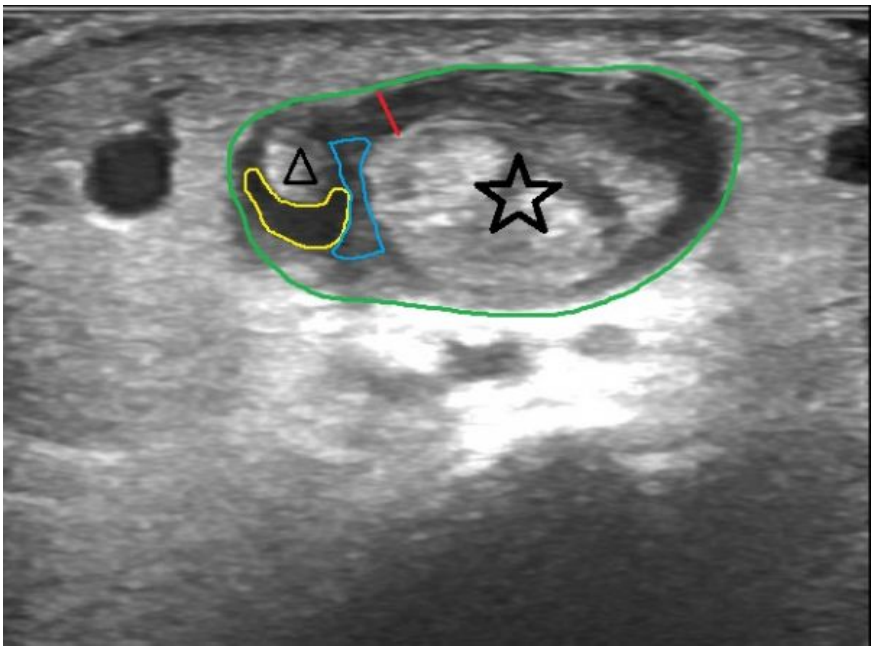
Multimodal ultrasonography provides objective diagnostic criteria for DQT, with extensor retinaculum thickness as the strongest discriminator. Strain elastography adds information independent of B-mode measurements. DQRTS outperformed individual parameters and, by combining multimodal ultrasound findings into a single score, offers a simple and reproducible tool for objective bedside diagnosis in routine practice. External validation in independent cohorts is warranted.

KEYWORDS

de Quervain tenosynovitis, ultrasonography, strain elastography, diagnostic score, random forest

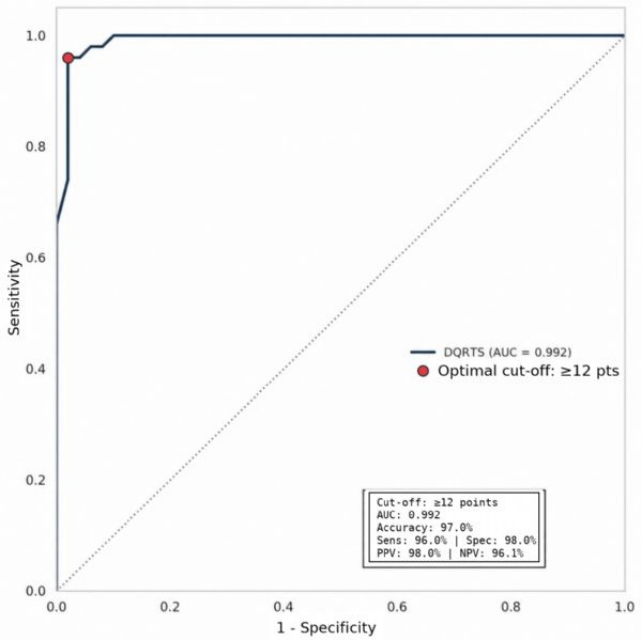
S-03 CONTINUED

B-mode ultrasonography of the first dorsal extensor compartment in de Quervain tenosynovitis



Transverse B-mode ultrasonographic image of the first dorsal extensor compartment in de Quervain tenosynovitis. The green line marks the boundary of the first extensor compartment, the red line the thickened extensor retinaculum, the blue area the intracompartmental septum, and the yellow area peritendinous fluid. The star (★) indicates the abductor pollicis longus (APL) tendon and the triangle (△) the extensor pollicis brevis (EPB) tendon.

ROC curve of the De Quervain Radiologic Diagnostic Score (DQRTS)



Receiver operating characteristic (ROC) curve of the De Quervain Radiologic Diagnostic Score (DQRTS) in the study sample (n=100). At a cut-off of >=12 points DQRTS achieved an area under the curve of 0.992 with 96.0% sensitivity and 98.0% specificity.

S-03 CONTINUED

Diagnostic performance of multimodal ultrasonography in de Quervain tenosynovitis.

Parameter	Patients (n=50)	Controls (n=50)	p
Extensor retinaculum thickness (mm), median [IQR]	1.00 [0.47]	0.40 [0.10]	<0.001
APL tendon thickness (mm), median [IQR]	4.05 [1.45]	2.60 [0.58]	<0.001
EPB tendon thickness (mm), median [IQR]	2.70 [0.98]	2.10 [0.40]	<0.001
Peritendinous fluid, n (%)	47 (94%)	3 (6%)	<0.001
Power Doppler vascularity, n (%)	14 (28%)	0 (0%)	<0.001
APL strain score, median [IQR]	4.0 [1.0]	2.0 [2.0]	<0.001
EPB strain score, median [IQR]	4.0 [2.0]	2.0 [1.0]	<0.001
Septation, n (%)	20 (40%)	20 (40%)	1.000

Parameter	AUC (95% CI)	Cut-off	Sensitivity
Extensor retinaculum thickness (mm), median [IQR]	0.985 (0.961-1.000)	>=0.70 mm	94%
APL tendon thickness (mm), median [IQR]	0.963 (0.925-1.000)	>=3.50 mm	82%
EPB tendon thickness (mm), median [IQR]	0.832 (0.752-0.913)	>=2.30 mm	84%
Peritendinous fluid, n (%)	-	-	-
Power Doppler vascularity, n (%)	-	-	-
APL strain score, median [IQR]	-	-	-
EPB strain score, median [IQR]	-	-	-
Septation, n (%)	-	-	-

S-03 CONTINUED

Parameter	Specificity
Extensor retinaculum thickness (mm), median [IQR]	94%
APL tendon thickness (mm), median [IQR]	96%
EPB tendon thickness (mm), median [IQR]	68%
Peritendinous fluid, n (%)	-
Power Doppler vascularity, n (%)	-
APL strain score, median [IQR]	-
EPB strain score, median [IQR]	-
Septation, n (%)	-

Values are median [IQR] or n (%). Continuous variables were compared with the Mann-Whitney U test and categorical variables with the Chi-square or Fisher's exact test. Strain patterns were coded ordinally (Type 1a=1 to 2b=4). $p<0.05$ was considered significant.

De Quervain Radiologic Diagnostic Score (DQRTS) scoring sheet.

No.	Parameter	Threshold	Points
1	Extensor retinaculum (sheath) thickness	>=0.70 mm	6
2	Peritendinous fluid	Present	6
3	APL tendon thickness	>=3.50 mm	4
4	EPB tendon thickness	>=2.30 mm	1
5	APL strain score	>=3 (Type 2a-2b)	1
6	EPB strain score	>=3 (Type 2a-2b)	1
7	Power Doppler vascularity	Present	1
TOTAL SCORE		Cut-off >=12	20

Weights were derived from the synthesis of Random Forest Gini importance ranking, ROC performance, and clinical rationale. A total score >=12 points classifies a case as de Quervain tenosynovitis (AUC=0.992, sensitivity 96%, specificity 98%, accuracy 97%).

S-04

Different Diseases, One Ultrasound Phenotype: Multiparametric Ultrasound Assessment of Sinusoidal Endothelial Injury Across VOD/SOS, Chemotherapy-Associated Sinusoidal Injury, and Post-Sepsis Hepatic Dysfunction

Andrzej Fedak[1], Krystian Mirowski[2], Jan Jamros[3], Agnieszka Czapska[3], Patrycja Mensah[4], Tadeusz Popiela[1]

[1] Chair of Radiology, Faculty of Medicine, Jagiellonian University Medical College, Kraków, Poland

[2] Chair of Gastroenterology, Faculty of Medicine, Jagiellonian University Medical College, Kraków, Poland

[3] Student Scientific Group, Chair of Radiology, Faculty of Medicine, Jagiellonian University Medical College, Kraków, Poland

[4] Chair of Hematology, Faculty of Medicine, Jagiellonian University Medical College, Kraków, Poland

AIM

To evaluate whether multiparametric ultrasound integrating HokUS-10, Doppler ultrasound, shear-wave elastography (SWE), and the Liver Stiffness Clinical Risk Score (L-SCR) identifies a common hemodynamic phenotype in patients with veno-occlusive disease/sinusoidal obstruction syndrome (VOD/SOS), chemotherapy-associated sinusoidal injury, and post-sepsis hepatic dysfunction.

METHODS

Between January 2024 and June 2026, 16 patients with clinical and ultrasound evidence of sinusoidal endothelial injury were identified. The cohort comprised eight patients with HSCT-related VOD/SOS (8/142 HSCT procedures; incidence 5.6%), seven patients with chemotherapy-associated sinusoidal injury, and one patient with persistent hepatic dysfunction following severe sepsis. VOD/SOS was diagnosed according to the European Society for Blood and Marrow Transplantation (EBMT) criteria. The remaining patients were included based on compatible clinical findings and HokUS-10 features consistent with sinusoidal congestion. Multiparametric ultrasound assessment comprised HokUS-10, Doppler ultrasound, shear-wave elastography (SWE), and the Liver Stiffness Clinical Risk Score (L-SCR). HSCT recipients underwent baseline and serial follow-up examinations.

RESULTS

Serial Doppler, SWE, and L-SCR abnormalities preceded overt clinical manifestations in several VOD/SOS patients. The most frequent findings were increased liver stiffness (14/16), reduced portal venous velocity (13/16), hepatic venous waveform flattening (12/16), abnormal hepatic arterial resistive index (11/16), and hepatomegaly (9/16). Ascites and jaundice were present in all patients. Seven VOD/SOS patients and the post-sepsis patient received defibrotide. Follow-up demonstrated improvement in portal hemodynamics, liver stiffness, L-SCR, and ascites among treatment responders. Chemotherapy-associated injury showed a more heterogeneous course, typically presenting approximately 60 days after treatment exposure. All groups demonstrated overlapping ultrasound features of sinusoidal congestion and portal hypertension.

CONCLUSION

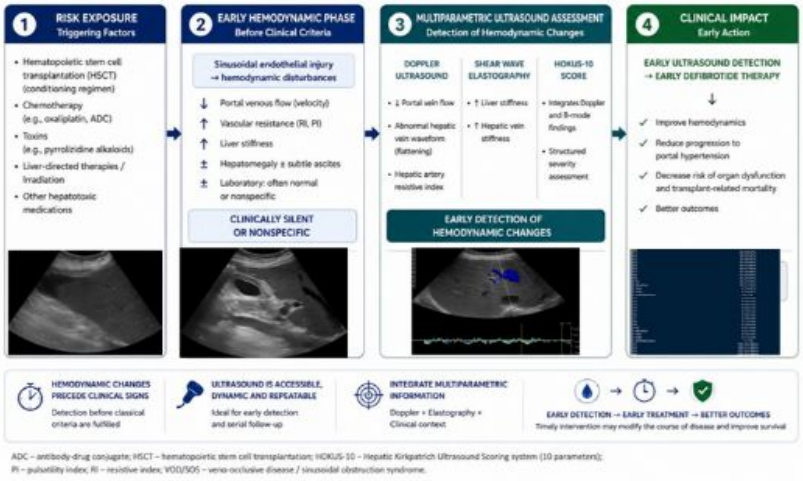
Structured multiparametric ultrasound may provide a reproducible bedside imaging approach for early detection, risk stratification, and longitudinal monitoring of sinusoidal endothelial injury. Despite different etiologies, VOD/SOS, chemotherapy-associated sinusoidal injury, and post-sepsis hepatic dysfunction share a common multiparametric ultrasound phenotype characterized by portal hemodynamic alterations, increased liver stiffness, and HokUS-10 abnormalities.

S-04 CONTINUED

KEYWORDS

Veno-occlusive disease, Multiparametric ultrasound, Doppler ultrasound, Shear-wave elastography, Sinusoidal obstruction syndrome

Figure 1. Multiparametric ultrasound as a bedside tool for early diagnosis of sinusoidal endothelial injury.



The proposed algorithm demonstrates how Doppler ultrasound, shear-wave elastography, and HokUS-10 complement each other in detecting early hemodynamic alterations preceding the clinical diagnosis of sinusoidal obstruction syndrome/veno-occlusive disease (VOD/SOS). The same ultrasound phenotype may also be observed in chemotherapy-associated sinusoidal injury and post-sepsis hepatic dysfunction, supporting multiparametric ultrasound as a practical bedside imaging approach for early diagnosis, risk stratification, and treatment monitoring.

Table 1. Multiparametric ultrasound findings

Parameter	n/N (%)
Increased liver stiffness	14/16 (87.5%)
Reduced portal venous velocity	13/16 (81.3%)
Hepatic venous waveform flattening	12/16 (75.0%)
Abnormal hepatic arterial RI	11/16 (68.8%)
Hepatomegaly	9/16 (56.3%)
Ascites	16/16 (100%)
Jaundice	16/16 (100%)

Explanation: Values are presented as the number of patients with each ultrasound finding (n), the total study population (N = 16), and the corresponding percentage. Ultrasound findings were assessed using multiparametric ultrasound, including Doppler ultrasound, shear-wave elastography, and HokUS-10.

S-05

Upper-Extremity Muscle Ultrasonography and Shear Wave Elastography for Sarcopenia Assessment: Preliminary Findings From a 70-Patient Cohort

Davut Ünsal Çapkan

Private MedicalPoint Hospital of the Radiology, Gaziantep, Turkey

BACKGROUND

Sarcopenia is a progressive skeletal muscle disorder characterised by reductions in muscle strength, mass, and physical performance. Although ultrasonography is increasingly used for muscle assessment, evidence regarding shear wave elastography (SWE) of upper-extremity muscles remains limited.

OBJECTIVE

To preliminarily evaluate biceps brachii and flexor digitorum superficialis (FDS) muscle thickness and SWE-derived stiffness in relation to sarcopenia as defined by the European Working Group on Sarcopenia in Older People 2 (EWGSOP2).

METHODS

This preliminary analysis included 70 adults aged >=65 years from an ongoing prospective observational study. Sarcopenia was assessed according to EWGSOP2 using SARC-F, handgrip strength, the five-times chair stand test, and bioelectrical impedance analysis. Biceps brachii and FDS muscle thickness were measured using B-mode ultrasonography, while muscle stiffness was quantitatively assessed using SWE. Participants were classified as normal (n = 28), probable sarcopenia (n = 27), or confirmed sarcopenia (n = 15)(Figure1).

RESULTS

Significant differences were observed among the normal, probable, and confirmed sarcopenia groups for clinical and ultrasonographic parameters (all $P<0.001$). Biceps muscle thickness decreased across groups (18.5±2.1, 16.6±1.9, and 13.5±1.8 mm), as did FDS muscle thickness (10.5±1.3, 9.4±1.2, and 7.9±1.0 mm). In contrast, biceps SWE increased from 14.9±2.7 to 18.6±3.0 and 25.1±4.1 kPa, while FDS SWE increased from 16.3±3.0 to 20.0±3.4 and 27.6±4.6 kPa, respectively. Reduced muscle thickness and increased SWE-derived stiffness paralleled sarcopenia severity, with FDS SWE showing marked discrimination across EWGSOP2 categories (Table 1).

CONCLUSION

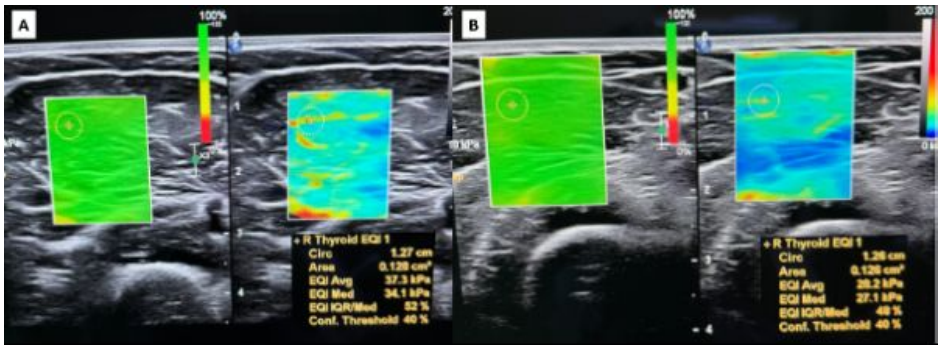
Preliminary findings suggest that upper-extremity ultrasonography combined with SWE may provide complementary quantitative information on muscle quantity and mechanical properties in older adults. FDS SWE appears particularly promising as a potential imaging biomarker for sarcopenia. Validation in the complete study cohort is warranted.

KEYWORDS

Sarcopenia, Ultrasonography, Elasticity Imaging Techniques, Muscle, Muscle Strength

S-05 CONTINUED

Figure 1



Shear wave elastography image of the biceps brachii muscle with the corresponding confidence map and region of interest placement.

Table 1

Variable	Normal	Probable Sarkopenia	Confirmed Sarkopenia	P value
Age (years)	68.1 ± 3.6	71.3 ± 4.4	75.2 ± 5.1	<0.001
SARC-F score	2.4 ± 1.3	4.5 ± 1.5	6.2 ± 1.4	<0.001
Handgrip strength (kg)	27.9 ± 6.8	17.4 ± 4.8	10.8 ± 3.7	<0.001
Chair stand test (s)	11.6 ± 2.2	16.8 ± 3.2	21.7 ± 4.3	<0.001
ASMI (kg/m²)	8.05 ± 1.05	7.43 ± 1.08	5.69 ± 0.76	<0.001
Biceps muscle thickness (mm)	18.5 ± 2.1	16.6 ± 1.9	13.5 ± 1.8	<0.001
Biceps SWE (kPa)	14.9 ± 2.7	18.6 ± 3.0	25.1 ± 4.1	<0.001
FDS muscle thickness (mm)	10.5 ± 1.3	9.4 ± 1.2	7.9 ± 1.0	<0.001
FDS SWE (kPa)	16.3 ± 3.0	20.0 ± 3.4	27.6 ± 4.6	<0.001

Clinical and Ultrasonographic Characteristics of the 70-Participant Preliminary Cohort According to EWGSOP2 Categories

S-06

Large Language Models for ACR TI-RADS Categorization and Thyroid Nodule Malignancy Prediction: A Pathology-Validated Study

Mahsima Gül Gümrükçü, Tuba Dalgalar Akkaya, Enes Gürün, Mesut Öztürk

Samsun University, Department of Radiology

AIM

To evaluate whether large language models (LLMs) can apply ACR TI-RADS to structured thyroid ultrasound findings and predict thyroid nodule malignancy.

METHODS

This retrospective study included 295 thyroid nodules with complete ACR TI-RADS features, radiologist-assigned TI-RADS category, and at least one size measurement. The cohort included 127 malignant and 168 benign nodules, with surgical pathology as the reference standard. For each nodule, de-identified ultrasound features, maximum nodule diameter, age, and sex were provided as text to GPT-5.6, Gemini 3.7 Flash, and Claude Opus 5. Each nodule was evaluated independently without access to the radiologist's TI-RADS category, pathology outcome, or other cases. Each model was asked to perform two separate tasks: (1) calculate the ACR TI-RADS score and category from the provided ultrasound features, and (2) separately estimate the probability of malignancy and classify the nodule as malignant or benign. Agreement with the radiologist-assigned TI-RADS category was assessed using weighted Cohen's kappa. Diagnostic performance was evaluated using sensitivity, specificity, and AUC.

RESULTS

Malignancy prediction yielded AUCs of 0.738, 0.764, and 0.761 for GPT-5.6, Gemini 3.7 Flash, and Claude Opus 5, respectively. The radiologist-assigned TI-RADS category showed a similar AUC of 0.767. At the default probability cutoff of 0.5, LLM sensitivity was 36.2-44.1% and specificity was 86.9-90.5%. In comparison, the radiologist-assigned TI-RADS TR4/5 threshold showed 87.4% sensitivity and 54.8% specificity. TI-RADS category agreement with the radiologist was 99.7% for GPT-5.6 and Gemini 3.7 Flash and 93.6% for Claude Opus 5 (κ = 0.93-1.00).

CONCLUSION

LLMs accurately reproduced ACR TI-RADS categorization from structured ultrasound findings, but their malignancy predictions showed no clear advantage over radiologist-assigned TI-RADS and operated at a more conservative threshold. LLMs may therefore be useful as structured decision-support aids rather than stand-alone diagnostic tools. Further prospective validation in larger, unselected populations is warranted before clinical implementation.

KEYWORDS

Thyroid nodule, ACR TI-RADS, Large language models, Artificial intelligence

S-06 CONTINUED

Table 1. LLM performance in ACR TI-RADS categorization and malignancy prediction

Model / Reference	TI-RADS agreement	Sensitivity	Specificity	AUC
GPT-5.6	99.7%	36.2%	90.5%	0.738
Gemini 3.7 Flash	99.7%	40.9%	89.3%	0.764
Claude Opus 5	93.6%	44.1%	86.9%	0.761
Radiologist-assigned TI-RADS (TR4/5)	-	87.4%	54.8%	0.767

Comparison of TI-RADS agreement and malignancy prediction performance of the three LLMs with radiologist-assigned TI-RADS.

S-07

Inter-View Variability Between Orthogonal Breast Ultrasound Images for Differentiating Benign and Malignant Lesions

Seyit Erol, Ahmet Baytok

Selcuk University Faculty of Medicine

AIM

To investigate whether changes in lesion roundness and contour irregularity between two orthogonal breast ultrasound views are associated with malignancy.

METHODS

This retrospective secondary analysis used the publicly available BUS-BRA dataset. Among 1,064 biopsy-proven breast lesions, 811 lesions with two paired ultrasound views were included (546 benign, 265 malignant). Expert-provided segmentation masks were used to calculate two scale-independent shape descriptors: roundness ($4\pi A/P^2$) and contour irregularity [1 - (convex hull perimeter/lesion perimeter)]. For each lesion, the absolute difference between the two views was calculated for both parameters. Benign and malignant lesions were compared using the Mann-Whitney U test, and discriminatory performance was assessed by receiver operating characteristic analysis. A secondary analysis was performed in BI-RADS 4 lesions.

RESULTS

Inter-view roundness variation was slightly higher in malignant than benign lesions (median, 0.061 vs 0.053; $p=0.033$), but showed limited discrimination (AUC=0.546). In contrast, contour irregularity variation was markedly greater in malignant lesions (0.031 vs 0.008; $p<0.001$), with an AUC of 0.772. Among 300 BI-RADS 4 lesions (121 benign, 179 malignant), contour irregularity variation remained significantly higher in malignant lesions (0.031 vs 0.015; $p<0.001$; AUC=0.660), whereas roundness showed no discriminatory value ($p=0.992$; AUC=0.500).

CONCLUSION

Malignant breast lesions demonstrate greater variation in contour irregularity between orthogonal ultrasound views. Inter-view contour variability may represent a simple quantitative marker of malignancy, including within BI-RADS 4 lesions.

KEYWORDS

Breast ultrasound, Breast lesions, Morphologic variability, Contour irregularity, BI-RADS

S-07 CONTINUED

Figure 1

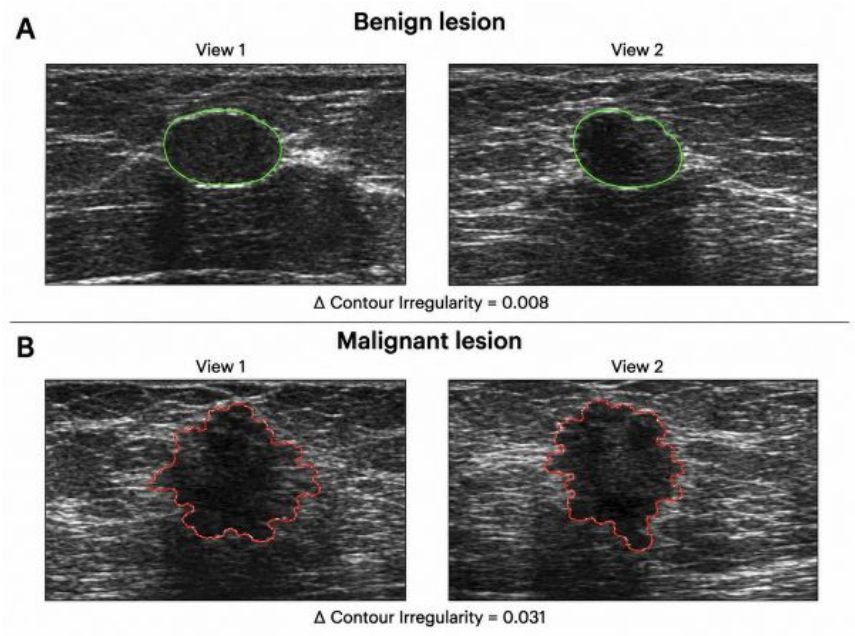


Figure 1. Representative paired ultrasound images of benign (A) and malignant (B) breast lesions. Expert-provided segmentation contours are overlaid. The benign lesion shows minimal inter-view contour variation (Δ=0.008), whereas the malignant lesion demonstrates greater contour variation (Δ=0.031).

Figure 2

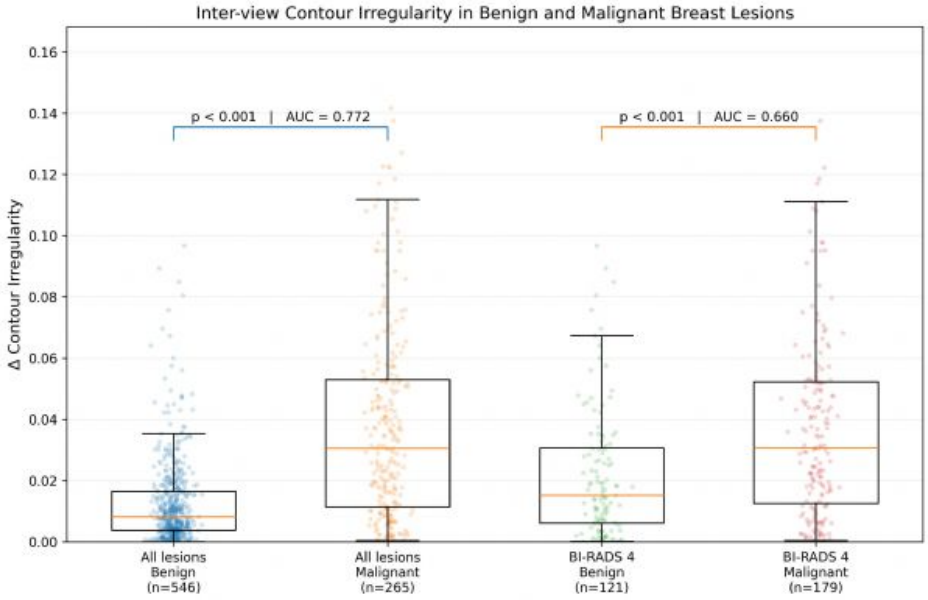


Figure 2. Inter-view contour irregularity differences between benign and malignant breast lesions. Malignant lesions showed significantly greater contour irregularity variation between paired orthogonal ultrasound views than benign lesions in the overall cohort (AUC=0.772; p<0.001). This difference remained significant in the BI-RADS 4 subgroup (AUC=0.660; p<0.001). Boxplots represent the distribution of absolute inter-view differences (Δ contour irregularity); individual observations are overlaid.

S-07 CONTINUED

Table 1. Inter-view shape variability in benign and malignant breast lesions

Analysis	Parameter	Benign (n)	Malignant (n)	Benign median (IQR)
All paired lesions	Roundness	546	265	0.053 (0.025-0.097)
All paired lesions	Contour irregularity	546	265	0.008 (0.004-0.016)
BI-RADS 4	Roundness	121	179	0.062 (0.027-0.108)
BI-RADS 4	Contour irregularity	121	179	0.015 (0.006-0.031)

Analysis	Parameter	Malignant median (IQR)	p	AUC
All paired lesions	Roundness	0.061 (0.031-0.113)	0.033	0.546
All paired lesions	Contour irregularity	0.031 (0.011-0.053)	<0.001	0.772
BI-RADS 4	Roundness	0.031 (0.011-0.053)	0.992	0.500
BI-RADS 4	Contour irregularity	0.031 (0.013-0.052)	<0.001	0.660

S-08

The Art of Seeing the Unseen: Ultrasound Pearls in the Detection of Elusive Parathyroid Adenomas

Sebam Sarıoğlu, Alper Özel

Şişli Hamidiye Etfal Training and Research Hospital Radiology Department

AIM

Ultrasound (US) plays a key role in preoperative localization of parathyroid adenomas (PAs). Nevertheless, around 6-16% of PAs are ectopically located along the embryological descent pathways or may show atypical sonographic features, leading to false negative results. In this case series, we aimed to demonstrate a spectrum of elusive PAs while highlighting the US pearls and pitfalls to look out for.

METHODS

Six cases of elusive PAs, confirmed by surgical histopathology and/or FNA-PTH washout, were retrospectively analysed for US features. All patients underwent multiparametric neck US (high-resolution B-mode, Color Doppler, elastography). A systematic scan was performed from the upper carotid space to the suprasternal fossa. Lesions were classified according to their anatomical location (intrathyroidal, paraesophageal, lower neck/thyrothymic, and suprasternal/mediastinal) and atypical sonographic features, including hyperechoic or dual-echo appearance, cystic degeneration, and lymph node mimicry.

RESULTS

Our series highlights the sonographic spectrum of elusive PAs:

1. Intrathyroidal PA: Mimicking a thyroid nodule; distinguished by a hypoechoic mass with a distinct capsule and feeding polar vessel.

2. Lipoadenoma: appears hyperechoic or isoechoic, mimics lipoma or thyroid tissue.

3. Cystic PA: shows extensive cystic degeneration, mimicking a thymic or congenital cyst, or a necrotic lymph node.

4. Atypical Hard Location- Paraesophageal PA: Located deep in the tracheoesophageal region, localized using Doppler US.

5. Hashimoto's Trap: Obscured by reactive lymph nodes and identified by its peripheral vascular pattern.

6. Ectopic Mediastinal PA: Missed on standard views, visualized through a caudal suprasternal approach in the anterior superior mediastinum.

CONCLUSION

Identifying elusive PAs is challenging especially in the presence of pitfalls and sonographic mimics. However, knowledge of embryological descent pathways, awareness of the atypical US features and adoption of a systematic scan protocol are crucial for recognizing elusive PAs. Ultrasound alone remains a valuable tool in turning the unseen into a reliable map for minimally invasive parathyroidectomy.

KEYWORDS

Parathyroid adenoma, Ultrasonography, Ectopic parathyroid

S-09

Sonographic Features Across the Histopathologic Spectrum of Non-Mass Breast Lesions: From Benignity to Invasive Carcinoma

Gülbanu Güner, Muhsin Ayhan, Sevde Nur Emir

Ümraniye Eğitim ve Araştırma Hastanesi, Radyoloji Ana Bilim Dalı, İstanbul

AIM

To investigate how the sonographic phenotype of non-mass breast lesions varies across the histopathologic spectrum from benignity to ductal carcinoma in situ (DCIS) and invasive carcinoma, and to identify sonographic features independently associated with carcinoma.

METHODS

Patients with non-mass breast lesions detected on ultrasound between January 2022 and December 2025 were retrospectively evaluated. Patients with prior breast cancer, age <18 years, no histopathologic confirmation, or unavailable stored ultrasound images were excluded. Among 141 patients, 147 lesions were classified as benign (n=108), DCIS (n=9), or invasive carcinoma (n=30). Stored images were reviewed in consensus by two breast radiologists with 9 and 4 years of experience, blinded to histopathology. Lesion size, hypoechoic area, architectural distortion, sonographic calcifications, multiple small cysts, ductal abnormalities, and posterior acoustic shadowing were recorded. Features were compared among groups, with trend analysis across the benign-DCIS-invasive carcinoma spectrum. Factors associated with carcinoma (DCIS + invasive carcinoma) were assessed by univariable and multivariable logistic regression.

RESULTS

Sonographic calcifications increased across benign, DCIS, and invasive carcinoma groups (14.8%, 44.4%, and 56.7%, respectively; $p<0.001$; p for trend<0.001). Architectural distortion differed among groups and was most frequent in benign lesions (89.8%, 44.4%, and 66.7%, respectively; $p<0.001$). On multivariable analysis, sonographic calcifications were independently associated with higher odds of carcinoma (adjusted OR=6.21; 95% CI: 2.50-15.43; $p<0.001$), whereas architectural distortion was independently associated with lower odds of carcinoma (adjusted OR=0.23; 95% CI: 0.08-0.63; $p=0.004$).

CONCLUSION

Sonographic features of non-mass breast lesions differed across the benign-DCIS-invasive carcinoma spectrum. Sonographic calcifications showed an increasing trend and were independently associated with carcinoma, whereas architectural distortion was frequent in benign lesions, which showed a high prevalence of fibrotic stromal changes and adenosis. These findings support collective interpretation of sonographic features rather than reliance on a single morphologic feature.

KEYWORDS

Breast, Ultrasonography, Non-mass lesion, Ductal carcinoma in situ, Invasive carcinoma

S-09 CONTINUED

Non-mass breast lesions across the histopathologic spectrum

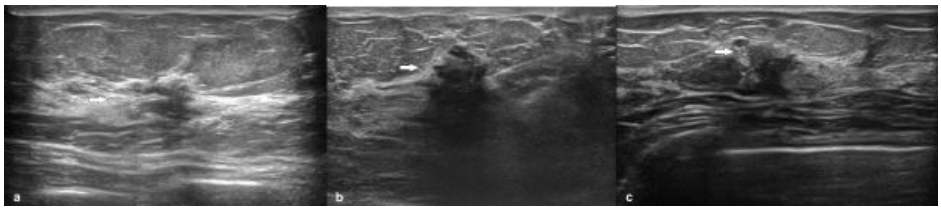


Figure 1. Representative ultrasound images of non-mass breast lesions across the histopathologic spectrum. (a) Benign lesion histopathologically diagnosed as sclerosing adenosis, demonstrating a hypoechoic area with associated architectural distortion (white arrow). (b) Ductal carcinoma in situ (DCIS), demonstrating parenchymal distortion with posterior acoustic shadowing (white arrow). (c) Invasive carcinoma, demonstrating a hypoechoic area with punctate echogenic foci suggestive of microcalcifications (white arrow).

S-10

Diagnostic Accuracy of Laryngeal Ultrasonography for Benign Vocal Fold Nodules in Children: Correlation With Fiberoptic-Flexible Laryngoscopy

Ahmet Adnan Cırık[1], Elif Dilara Topcuoğlu[2], Ceren Aksoy Koçak[5], Mehmet Öztürk[3], Neşe Torun[1], Ömer Erdur[4]

[1] University of Health Sciences Umraniye Training and Research Hospital, Department of Otorhinolaryngology

[2] University of Health Sciences Umraniye Training and Research Hospital, Department of Radiology

[3] Selcuk University School of Medicine, Department of Radiology

[4] Liv Hospital Ulus, Department of Otorhinolaryngology

[5] Konya City Hospital, Department of Otorhinolaryngology

AIM

Fiberoptic-flexible laryngoscopy (FFL) is the reference standard for assessing pediatric dysphonia but is invasive and poorly tolerated by young children. Laryngeal ultrasonography (LUS) has been proposed as a non-invasive alternative. This study evaluated the diagnostic accuracy of LUS against FFL for detecting vocal fold nodules in children referred for dysphonia.

METHODS

Forty-nine children (31 males, 18 females; mean age 7.5 ± 2.6 years, range 3-13) were independently enrolled at two tertiary referral centers and underwent both FFL, performed by an ear-nose-throat physician, and LUS, performed blindly by a radiologist unaware of FFL findings. For each vocal fold, nodule presence, laterality, and size (longest axis, mm) were recorded on LUS and compared with FFL findings taken as the reference standard. Sensitivity, specificity, positive and negative predictive values, and overall agreement were calculated.

RESULTS

FFL identified vocal fold nodules in 33 of the 49 children (67.3%); 16 children had normal vocal folds. Compared with FFL, LUS showed a sensitivity of 90.9%, specificity of 81.3%, positive predictive value of 90.9%, negative predictive value of 81.3%, and overall accuracy of 87.8% (30 true positives, 13 true negatives, 3 false positives, 3 false negatives).

CONCLUSION

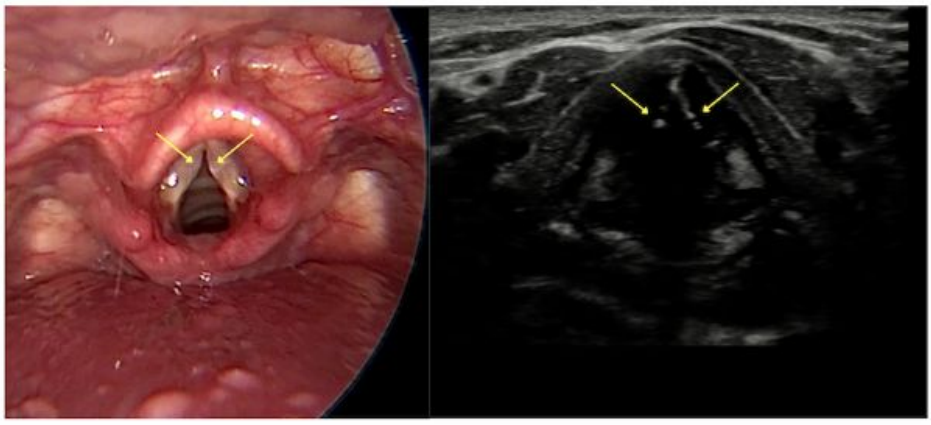
LUS showed good correlation with FFL for detecting vocal fold nodules in children, supporting its role as a non-invasive, well-tolerated adjunct or alternative to endoscopy in pediatric dysphonia work-up. Given the modest sample size and the use of independent examiners and equipment at each site, larger studies with harmonized, blinded protocols are needed to confirm inter-observer and inter-center reliability of LUS measurements.

KEYWORDS

fiberoptic laryngoscopy, laryngeal ultrasonography, pediatric dysphonia, vocal fold nodule

S-10 CONTINUED

Figure



Fiberoptic-flexible laryngoscopy (left) and laryngeal ultrasonography (right) images of 8-year-old male patient. Yellow arrows indicate bilateral milimetric vocal fold nodules on each.

S-12

Diagnostic Adequacy and Safety of Ultrasound Guided Tru-Cut Biopsy for Pleural Based Lung Lesions

Murat Ozogul

Department of Radiology, Istanbul Training and Research Hospital, Istanbul Türkiye

AIM

Ultrasound (US)-guided percutaneous biopsy offers real time visualization of the needle trajectory without ionizing radiation and may be particularly advantageous for peripheral lung lesions in contact with the pleural surface. This study aimed to evaluate the diagnostic adequacy and safety of US-guided tru-cut biopsy for pleural-based lung lesions.

METHODS

We retrospectively evaluated 72 patients who underwent US-guided tru-cut biopsy of pleural based lung lesions between January 2024 and June 2026. All procedures were performed using an 18-G tru-cut biopsy needle, and at least two core tissue samples were obtained from each lesion. Demographic characteristics, lesion size, pleural contact length, histopathological findings, and procedure related complications were recorded. Pneumothorax, hemoptysis, and changes in hematocrit levels were assessed. Post procedural posteroanterior chest radiography was obtained at 1 hour, and hematocrit was reassessed at 4 hours.

RESULTS

The mean age was 71 ± 5 years; 44 patients (61.1%) were male and 28 (38.9%) were female. The mean maximum long-axis diameter of the lesions was 56.4 mm (range, 21-142 mm), and the mean pleural contact length was 34 ± 10 mm. Histopathology demonstrated malignancy in 61 patients (84.7%) and benign findings in 11 patients (15.3%). Adequate tissue for histopathological evaluation was obtained in all patients, corresponding to a diagnostic adequacy rate of 100%. Pneumothorax occurred in 2 patients (2.8%); both were asymptomatic and managed conservatively without chest tube placement. A decrease in hematocrit was observed in 6 patients (8.3%) without clinically significant consequences or need for additional intervention. No hemoptysis or major procedure-related complications occurred.

CONCLUSION

US-guided tru-cut biopsy is a safe and reliable sampling technique for peripheral lung lesions in contact with the pleural surface, providing high diagnostic adequacy with a low complication rate while avoiding ionizing radiation.

KEYWORDS

Ultrasound guided biopsy, Tru-cut biopsy, Lung lesions, Pleural based lesions, Percutaneous biopsy

S-12 CONTINUED

Figure 1.

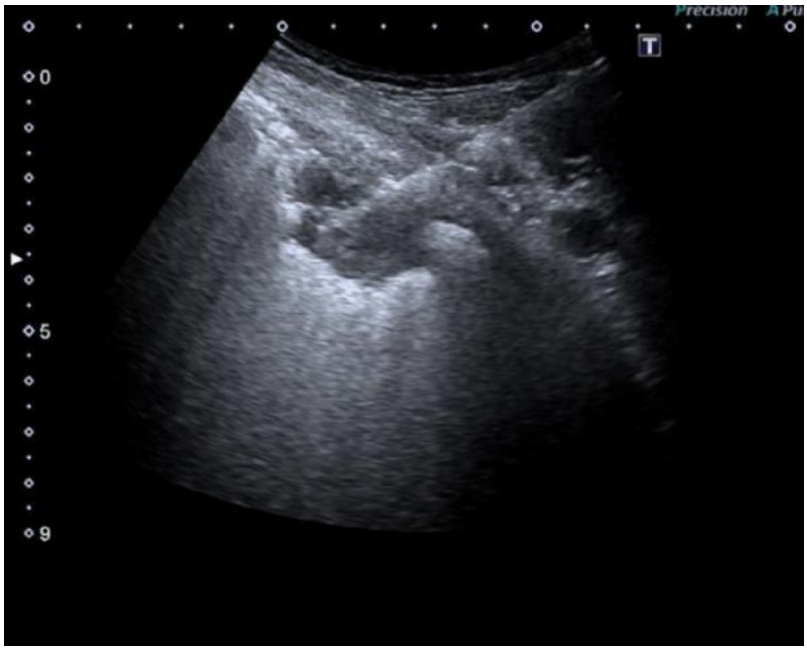


Figure 1. Ultrasound image demonstrating a pleural based peripheral lung lesion during tru-cut biopsy, with the needle tip positioned within the lesion.

S-12 CONTINUED

Table 1:Patient, lesion, procedural, and outcome characteristics

Variable	Value
Patient and lesion characteristics	
Number of patients	72
Age, years	71 ± 5
Male	44 (61.1%)
Female	28 (38.9%)
Maximum long-axis diameter, mm	56.4 (21-142)
Pleural contact length, mm	34 ± 10
Histopathological findings	
Malignant	61 (84.7%)
Benign	11 (15.3%)
Procedural characteristics	
Biopsy needle	18 G
Core tissue samples	>=2 per lesion
Diagnostic and safety outcomes	
Diagnostically adequate biopsy	72 (100%)
Pneumothorax	2 (2.8%)
Hematocrit decrease	6 (8.3%)
Hemoptysis	0 (0%)
Major procedure related complications	0 (0%)

Data are presented as mean ± standard deviation, n (%), or range, as appropriate. US, ultrasonography.

S-13

Multiparametric Liver Ultrasonography in Systemic Sclerosis

Atiye Cenay Karabörk Kılıç[1], Ibrahim Vasi[2], Ece Altay[1], Ibrahim Karaduman[2], Semih Güllüoğlu[1], Mahi Nur Cerit[1], Halit Nahit Şendur[1], Abdulsamet Erden[2], Suna Özhan Oktar[1]

[1] Department of Radiology, Gazi University Faculty of Medicine, Ankara, Turkey.

[2] Division of Rheumatology, Department of Internal Medicine, Gazi University Faculty of Medicine, Turkey.

AIM

Hepatic involvement in systemic sclerosis (SSc) has been described but remains poorly defined, as liver abnormalities may be subtle or clinically silent, and conventional tests may miss early changes. Multiparametric ultrasonography enables non-invasive assessment of liver tissue characteristics. Shear-wave elastography (SWE) quantifies liver stiffness; ultrasound attenuation technology (USAT), the hepatorenal index (HRI), and liver tissue index (LTI) evaluate hepatic steatosis. This study aimed to assess liver stiffness and steatotic characteristics in SSc patients using multiparametric ultrasonography and compare them with those of healthy controls.

METHODS

In this study, 34 SSc patients and 31 healthy controls underwent liver ultrasonography using a Mindray Resona R9 system. The protocol included SWE, USAT, HRI, and LTI measurements. Liver size and steatosis grade were recorded. ALT, ALP, GGT, albumin, platelet count, and LDL were also recorded.

RESULTS

SWE values were significantly higher in SSc patients than in controls (7.39 (2.3) vs 4.79 (1.27) kPa, $p < 0.001$). HRI (1.22 (0.48) vs 1.05 (0.25), $p = 0.001$), LTI (1.88 (1.04) vs 1.24 (0.46), $p < 0.001$), and USAT (0.59 (0.12) vs 0.54 (0.09), $p = 0.016$) were also significantly elevated in SSc. ALP levels were higher in SSc patients (87.7 ± 28.5 vs 55.5 ± 17.1 IU/L, $p < 0.001$), whereas ALT, GGT, albumin, platelet count, and LDL were similar. Hepatic steatosis was more frequent in SSc (47.1% vs 22.6%), but the difference was not statistically significant ($p = 0.068$).

CONCLUSION

Multiparametric liver ultrasonography showed increased liver stiffness and altered parenchymal indices in SSc despite largely normal routine liver biochemistry, supporting its role as a non-invasive tool for detecting subclinical hepatic involvement. Multiparametric liver ultrasonography may have a role for detecting subclinical hepatic involvement in SSc patients.

KEYWORDS

Systemic sclerosis, Liver stiffness, Shear-wave elastography, Hepatic steatosis, Multiparametric ultrasonography

S-13 CONTINUED

Comparison of Ultrasonographic Liver Parameters Between Patients With Systemic Sclerosis and Healthy Controls

Ultrasonographic parameter	SSc group (n = 34)	Control group (n = 31)	p value
Liver stiffness measured by SWE, kPa	7.39 (2.30)	4.79 (1.27)	<0.001
Hepatorenal index	1.22 (0.48)	1.05 (0.25)	0.001
Liver tissue index	1.88 (1.04)	1.24 (0.46)	<0.001
USAT value, dB/cm/MHz	0.59 (0.12)	0.54 (0.09)	0.016

S-14

Does Raising Colour Doppler PRF Improve Ultrasound Detection of Intrarenal Calculi? A Before-After Study

Andelib Babatürk

Ankara Güven Hospital, Department of Radiology, Ankara, Turkey

AIM

Raising colour Doppler pulse repetition frequency (PRF) suppresses narrow-band parenchymal flow while the broadband twinkling artefact of calculi persists. This manoeuvre has been described but not tested for diagnostic accuracy. We compared ultrasound (US) detection of intrarenal calculi before and after its routine adoption, with CT as reference standard.

METHODS

Retrospective single-centre before-after cohort study. Patients undergoing abdominal or renal US for any indication and non-contrast CT within 7 days were identified in two periods (A, before adoption; B, after) separated by a one-month transition. In Period B, scale/PRF was raised until parenchymal flow was suppressed and only twinkling persisted. Only US-before-CT examinations were included, avoiding review bias. All examinations were performed and reported by one radiologist (ACUSON Sequoia, 5C1). The analysis unit was the kidney; CT-positivity required at least one intrarenal calculus >=1 mm. Wilson and Newcombe 95% confidence intervals (CI) and Fisher's exact test were used.

RESULTS

198 patients (395 kidneys) were analysed: Period A 113 patients/226 kidneys, Period B 85/169. Periods were comparable in age, sex, US-CT interval and CT-positive kidney rate (14.2% vs 13.6%, p=1.00). Sensitivity (primary endpoint) was 62.5% (CI 45.3-77.1) versus 73.9% (53.5-87.5); difference 11.4 points (CI -13.6 to +33.3, p=0.40). Specificity rose from 93.3% to 99.3%, difference 6.0 points (CI 1.9-10.5, p=0.005), with false positives falling from 6.7% to 0.7%. PPV increased from 60.6% to 94.4%. For calculi under 5 mm, sensitivity was 56.0% versus 66.7%.

CONCLUSION

Adoption of the high-PRF technique was associated with significantly higher specificity and PPV, whereas the sensitivity gain was not significant. This design cannot separate the Doppler setting from changes in observer attention; a within-patient paired study is warranted.

REFERENCES

Bacha R, et al. J Med Ultrasound. 2019;27(1):13-18.

Cunitz BW, et al. J Endourol. 2017;31(11):1123-1130.

Laher AE, et al. Eur J Emerg Med. 2020;27(1):13-20.

KEYWORDS

Twinkling artefact, Pulse repetition frequency, Kidney calculi

S-16

Beyond Gray-Scale Ultrasound: The Role of Ultramicroangiography and Elastography in Parathyroid Adenoma Diagnosis

Ayşe Arı[1], Ahmet Görgel[2], Ahmet Baytok[1]

[1] Department of Radiology, Faculty of Medicine, Selcuk University, Konya, Türkiye

[2] Department of Endocrinology and Metabolism, Faculty of Medicine, Selcuk University, Konya, Türkiye

AIM

To evaluate the diagnostic value of ultramicroangiography (UMA), quantified using color pixel percentage (CPP), and elastography in parathyroid adenomas (PAs), and to investigate their ability to differentiate PAs from cervical lymph nodes (LNs).

MATERIALS AND METHODS

This prospective study included 33 patients with biochemical suspicion of primary hyperparathyroidism who underwent diagnostic neck ultrasonography. Suspected PAs were evaluated using UMA and its subtraction technique (sUMA), with microvascularity quantitatively assessed using CPP. Elastography measurements were obtained in kilopascals (kPa). Three measurements were performed for each lesion, and mean values were calculated. Corresponding cervical LNs served as control lesions. PAs were confirmed by surgical histopathology or concordant scintigraphic findings. Imaging findings were compared between PAs and LNs. Receiver operating characteristic (ROC) analysis was performed to determine the diagnostic performance and optimal CPP cutoff value.

RESULTS

CPP values obtained from sUMA were significantly higher in PAs than in cervical LNs (31.88 ± 15.35 vs 8.41 ± 6.52, $p < 0.001$), indicating increased and more organized microvascularity in PAs. ROC analysis demonstrated excellent diagnostic performance of CPP for differentiating PAs from LNs, with an area under the curve (AUC) of 0.956 (95% CI: 0.907-0.993). At an optimal cutoff value of 15, CPP showed a sensitivity of 93.9%, specificity of 87.9%, and accuracy of 90.9%. Elastography demonstrated significantly lower stiffness values in PAs than in cervical LNs ($p < 0.05$), indicating that PAs were significantly softer. The combined use of UMA and elastography improved diagnostic accuracy compared with gray-scale ultrasonography alone.

CONCLUSION

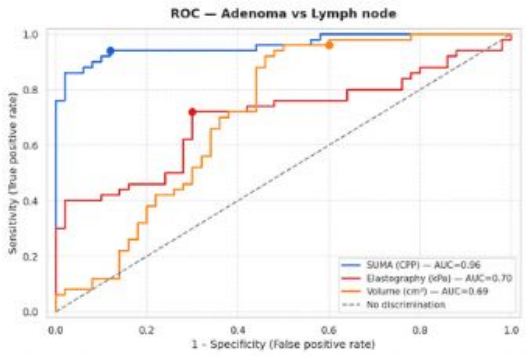
UMA with quantitative CPP assessment and elastography are valuable, non-invasive, contrast-free techniques for differentiating PAs from cervical LNs. UMA provides excellent quantitative assessment of microvascularity, while elastography offers complementary information regarding tissue stiffness. Their combined use may improve diagnostic confidence and facilitate more accurate characterization of parathyroid lesions.

KEYWORDS

Parathyroid adenoma, Ultra-Micro Angiography, color pixel percentage, elastography

S-16 CONTINUED

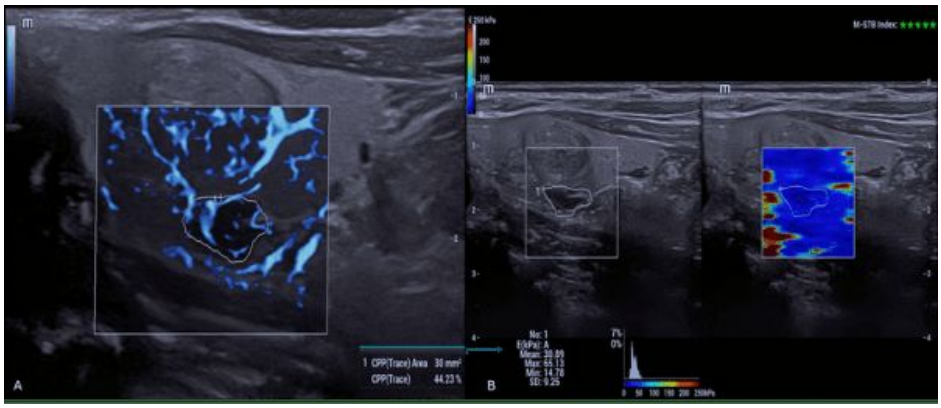
Figure 2. ROC curve analysis for the discrimination of parathyroid adenoma and cervical lymph nodes based on SUMA-CPP, elastography, and volume measurements.



ROC summary at Youden's optimal cutoff

Metric	AUC	Cutoff	Sens.	Spec.	Accuracy
SUMA (CPP)	0.96	15.00	0.94	0.88	0.91
Elastography (kPa)	0.70	23.77	0.72	0.70	0.71
Volume (cm³)	0.69	0.09	0.94	0.39	0.67

Figure1.Multiparametric Ultrasound Evaluation of a Parathyroid Adenoma



Parathyroid adenoma of the left thyroid lobe inferior pole in a 36-year-old woman. A, sUMA imaging demonstrating vascularity in the lesion, with CPP value of 44.23%. B, Shear Wave Elastography demonstrates a heterogeneous appearance with a quantitative mean stiffness value of 30.89 kPa.

Table II. Comparison of imaging parameters between parathyroid adenomas and cervical lymph nodes.

Metric	Parathyroid adenoma (Mean ± SD)	Lymph node (Mean ± SD)	Wilcoxon p
sUMA(CPP)	31.88 ± 15.35	8.41 ± 6.52	<0.001
Volume(cm³)	0.76 ± 0.82	0.34 ± 0.37	0.025

S-16 CONTINUED

Table I. Baseline characteristics of patients

Variable	Value
Female/Male sex	29 (87.9%) / 4 (12.1%)
Age (years), mean ± SD (range)	53.48 ± 12.06 (21-77)
Urolithiasis	6 (18.2%)
Adenoma location (Right/Left/Intrathyroidal)	19 (57.6%) / 13 (39.4%) / 1 (3.0%)
DEXA status (Normal/Osteopenia/Osteoporosis)	9 (27.3%) / 13 (39.4%) / 11 (33.3%)
Tc-99m MIBI (Positive/Negative)	28 (84.8%) / 5 (15.2%)
Ultrasound echogenicity (Hypo-/Isoechoic)	31 (93.9%) / 2 (6.1%)

S-17

Multiparametric Ultrasound Evaluation of Parotid Gland Stiffness and Microvascularity in Adults Living With HIV

Serkan Arıbal, Tanju Kisbet, Taha Oğuz Keklikoğlu, Kaan Işın, Hakan Önder

University of Health Sciences Türkiye, Prof. Dr. Cemil Taşcıoğlu City Hospital, Clinic of Radiology, İstanbul, Türkiye

AIM

To compare parotid gland stiffness and microvascularity between adults living with HIV (PLWH) and healthy controls using Sound Touch Elastography (STE) and Subtraction Ultra-Micro Angiography (sUMA), and to explore clinical and laboratory correlates.

METHODS

This prospective single-centre case-control study included 80 PLWH and 80 age-comparable healthy controls. Bilateral parotid examinations were performed using a Mindray Resona R9 ultrasound system with an L15-3WU linear probe. Parotid stiffness was measured by STE and microvascularity by sUMA; right, left, and overall mean values were calculated per subject. Between-group comparisons used the Mann-Whitney U test with Hodges-Lehmann median differences. Correlates within PLWH were assessed using Spearman correlation and multivariable linear regression. Representative images are provided in Figure 1.

RESULTS

PLWH and controls were comparable in age and smoking status, while BMI was lower in PLWH. Overall parotid stiffness, calculated as the mean of both glands, was higher in PLWH than in controls (13.70 vs 8.49 kPa; median difference +4.90 kPa; $p<0.001$). Overall sUMA vascularity index was also higher in PLWH (7.62% vs 3.10%; median difference +3.65 percentage points; $p<0.001$). In PLWH, mean elastography correlated inversely with ART duration and age; however, no independent predictor of elastography was identified. For mean sUMA, BMI was an independent inverse predictor ($\beta=-0.555$, $p<0.001$), whereas CD8+ T-cell count was an independent positive predictor ($\beta=+0.003$, $p=0.045$; adjusted $R^2=0.183$).

CONCLUSION

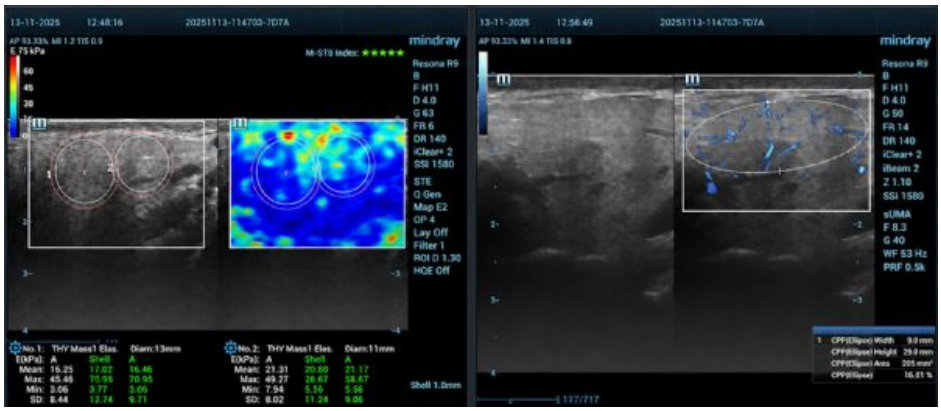
Parotid STE and sUMA demonstrated increased stiffness and microvascularity in PLWH, consistent with prior elastographic findings in HIV-related parotid involvement (1) and suggesting diffuse glandular alterations detectable by multiparametric ultrasound (2). The association between sUMA and CD8+ T-cell count may reflect a microvascular imaging signal linked to immune activity (3), although longitudinal and clinicopathological validation is required.

KEYWORDS

Elastography, Microvascular imaging, HIV

S-17 CONTINUED

Figure 1



Representative parotid ultrasound images from a person living with HIV. Left panel: Sound Touch Elastography (STE) colour map demonstrating elevated parenchymal stiffness, with ROI mean values ranging from 16.25 to 21.31 kPa and an M-STB quality index of 5 stars. Right panel: Subtraction Ultra-Micro Angiography (sUMA) showing increased parenchymal microvascularity, with a vascularity index of 16.01%.

S-18

Size Matters: Malignancy Risk of ACR-TIRADS 3 Thyroid Nodules in a 15-Year Cohort

Aysegul Gormez, Betul Uzunoglu

Radiology, Yeditepe University, Istanbul,Turkey

AIM

Management of ACR-TIRADS 3 thyroid nodules remains challenging in clinical practice. These nodules are generally considered low risk and are usually followed rather than biopsied. However, the actual malignancy risk and clinical behavior of TIRADS 3 nodules in real-world cohorts remain uncertain. This study aimed to evaluate the malignancy rate and size-related characteristics of ACR-TIRADS 3 thyroid nodules.

METHODS

This retrospective single-center study included thyroid nodules with histopathological confirmation evaluated between January 2007 and January 2025. Ultrasound examinations were reviewed and nodules were classified according to the ACR-TIRADS guideline. Nodules categorized as ACR-TIRADS 3 were included in the analysis. Patient age and nodule size were compared between benign and malignant nodules using the Mann-Whitney U test. Nodules were also evaluated according to size subgroups (<10 mm, 10-20 mm, >20 mm). Ultrasound features were compared using chi-square or Fisher's exact tests.

RESULTS

Among 1044 thyroid nodules, 151 (14.5%) were classified as ACR-TIRADS 3. Of these nodules, 137 (90.7%) were benign and 14 (9.3%) were malignant. Malignant TR3 nodules were significantly larger than benign nodules (median 26.5 mm vs 15 mm, p=0.001), whereas patient age did not differ significantly between groups (p=0.765). Malignancy distribution differed significantly across size categories (<10 mm, 10-20 mm, >20 mm; p=0.021), with higher malignancy rates observed in nodules larger than 20 mm. No significant association was observed between malignancy and the evaluated ultrasound features.

CONCLUSION

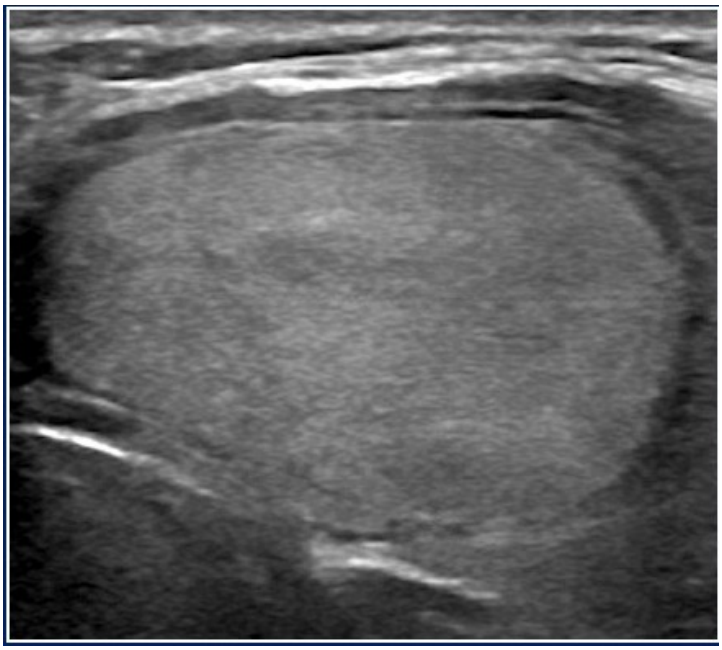
ACR-TIRADS 3 nodules demonstrated a higher malignancy rate than generally expected. Within this category, larger nodules showed a higher likelihood of malignancy, suggesting that nodule size may be an important factor in clinical decision-making for this intermediate-risk group.

KEYWORDS

Thyroid nodules, TIRADS, ultrasound, malignancy risk

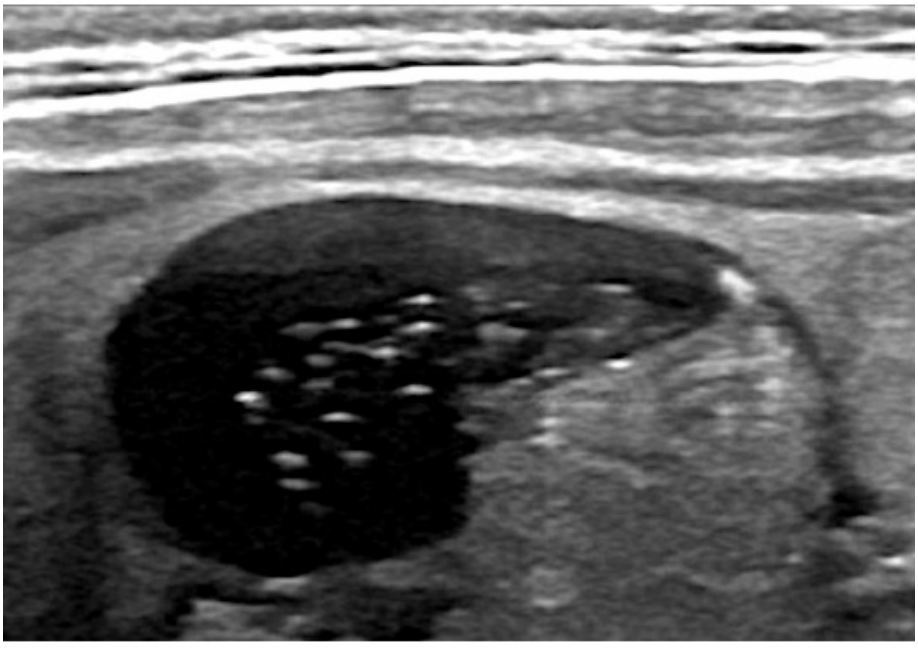
S-18 CONTINUED

Figure-1



Thyroid nodule with a size of 30x18mm in a 48-year-old woman. The nodule is solid, isoechoic, smoothly marginated, wider than tall, with no echogenic foci or calcifications. Classified as ACR TI-RADS 3, the nodule was pathologically confirmed as papillary thyroid carcinoma.

Figure-2



Thyroid nodule with a size of 24x10mm in a 40-year-old woman. The nodule is predominantly cystic with an eccentric isoechoic solid component, smooth margins, a thin hypoechoic halo, and a wider-than-tall shape. Classified as ACR TI-RADS 3, the nodule was pathologically confirmed as follicular thyroid carcinoma.

S-19

Optic Nerve Sheath Diameter and Central Retinal Artery Resistive Index in Hyponatraemia: A Sonographic Case-Control Study

Erdem Özkan

Department of Radiology, Kastamonu Training and Research Hospital, Kastamonu, Türkiye

AIM

Hyponatraemia induces osmotic cerebral oedema, and optic nerve sheath diameter (ONSD) has been proposed as a non-invasive marker of the resulting intracranial pressure rise, although published results conflict1,2 and rarely account for anatomical variability. Whether orbital arterial resistance changes in parallel is unknown. We assessed ONSD, the ONSD-to-eyeball transverse diameter ratio (ODR) and central retinal artery (CRA) resistive index.

METHODS

In this case-control study, 41 consecutive adults with laboratory-confirmed hyponatraemia (serum sodium <135 mmol/L) and 43 normonatraemic controls underwent orbital ultrasonography on the day of sodium sampling. Hyponatraemia was graded as moderate (125-134 mmol/L) or profound (<125 mmol/L)3. ONSD and eyeball transverse diameter were measured 3 mm behind the globe bilaterally with a high-frequency linear probe; CRA resistive index (RI) was recorded. Both eyes were averaged. Vitreoretinal surgery, glaucoma, optic neuropathy, intracranial pathology, cirrhosis and renal failure were excluded. Institutional ethics committee approval was obtained.

RESULTS

Age and sex were comparable ($p=0.121$; $p=0.803$). ONSD did not differ between groups (6.05±0.91 vs 6.09±0.70 mm, $p=0.835$), nor did ODR (0.264±0.040 vs 0.267±0.032, $p=0.738$), and neither correlated with serum sodium. CRA RI was higher in patients (0.667±0.053 vs 0.615±0.050, $p<0.001$; Cohen's $d=1.02$) and increased stepwise with severity (Table 1, Figure 1; Jonckheere-Terpstra $p<0.001$). Sodium correlated inversely with RI ($\rho=-0.493$, $p<0.001$), which persisted within the hyponatraemic group ($\rho=-0.407$, $p=0.008$) and after adjustment for age and sex ($p<0.001$). AUC was 0.761 for RI versus 0.475 for ONSD (Figure 2).

CONCLUSION

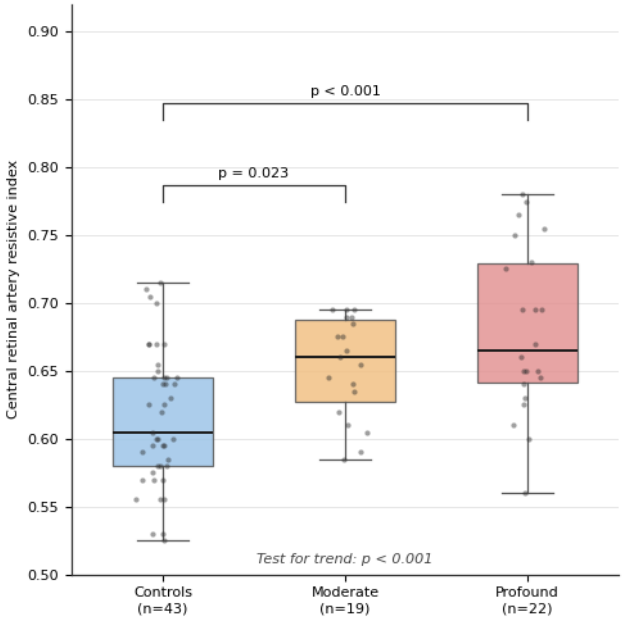
ONSD and ODR were unrelated to serum sodium, whereas CRA RI increased in parallel with the severity of hyponatraemia, independently of age and sex. Acute and chronic cases were indistinguishable, possibly explaining the absent sheath dilatation. The RI rise may reflect osmotically mediated changes in orbital vascular tone rather than raised intracranial pressure. Larger studies incorporating vascular risk profiling are warranted.

KEYWORDS

hyponatraemia, optic nerve sheath diameter, orbital ultrasonography, central retinal artery, resistive index

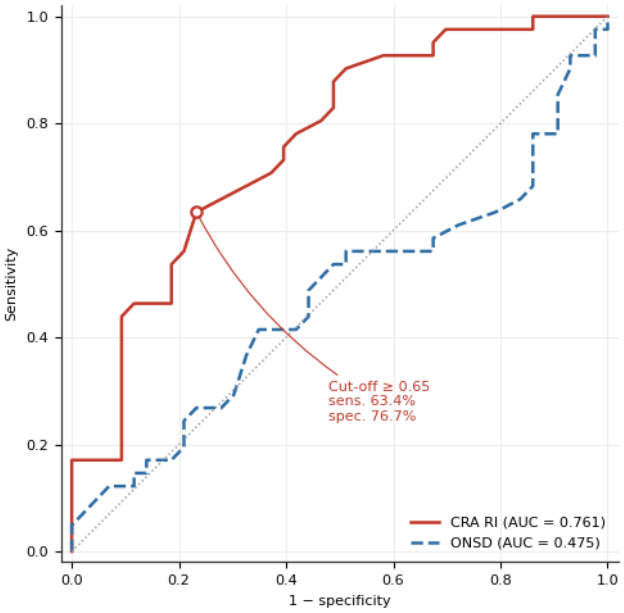
S-19 CONTINUED

Central retinal artery resistive index by hyponatraemia severity



Central retinal artery resistive index in controls (n=43), moderate hyponatraemia (125-134 mmol/L, n=19) and profound hyponatraemia (<125 mmol/L, n=22). Boxes show the median and interquartile range, whiskers 1.5×IQR, and individual measurements are overlaid. p values are Dunn post hoc comparisons with Bonferroni correction; Jonckheere-Terpstra test for trend p<0.001.

ROC curves for CRA resistive index and optic nerve sheath diameter



Receiver operating characteristic curves for central retinal artery resistive index (CRA RI) and optic nerve sheath diameter (ONSD) in discriminating hyponatraemic patients (n=41) from normonatraemic controls (n=43). The marked point indicates the Youden-optimal cut-off for the resistive index.

S-19 CONTINUED

Table 1. Orbital ultrasound and Doppler findings in hyponatraemic patients and normonatraemic controls

Parameter	Controls (n=43)	Moderate hyponatraemia 125-134 mmol/L (n=19)	Profound hyponatraemia <125 mmol/L (n=22)
Age (years)	67.4 ± 10.6	69.6 ± 13.5	75.4 ± 15.0
Female sex, n (%)	27 (62.8)	11 (57.9)	12 (54.5)
Serum sodium (mmol/L)	139.1 ± 1.4	129.6 ± 2.8	119.3 ± 3.0
ONSD (mm)	6.09 ± 0.70	6.20 ± 1.01	5.93 ± 0.83
ODR (ONSD/ETD)	0.267 ± 0.032	0.269 ± 0.042	0.259 ± 0.039
Optic nerve diameter (mm)*	3.11 ± 0.38	3.38 ± 0.38	3.22 ± 0.59
Eyeball transverse diameter (mm)	22.88 ± 1.18	23.06 ± 1.53	22.91 ± 1.58
CRA resistive index	0.615 ± 0.050	0.653 ± 0.037	0.680 ± 0.061

Parameter	p value	AUC (95% CI)
Age (years)	0.121	_
Female sex, n (%)	0.803	_
Serum sodium (mmol/L)	<0.001	_
ONSD (mm)	0.655	0.475 (0.352-0.601)
ODR (ONSD/ETD)	0.516	0.455 (0.335-0.582)
Optic nerve diameter (mm)*	0.060	0.630 (0.498-0.753)
Eyeball transverse diameter (mm)	0.844	_
CRA resistive index	<0.001	0.761 (0.654-0.861)

Values are mean ± SD unless stated. Groups were compared with the Kruskal-Wallis test (continuous variables) or the chi-square test (categorical variables); AUC refers to the discrimination of hyponatraemic patients (n=41) from controls, with 95% CI derived from bootstrap resampling. For CRA resistive index, the Youden-optimal cut-off was >=0.65 (sensitivity 63.4%, specificity 76.7%); the Jonckheere-Terpstra test for trend gave p<0.001; Dunn post hoc comparisons with Bonferroni correction: controls vs profound p<0.001, controls vs moderate p=0.023, moderate vs profound p=0.97. ONSD, optic nerve sheath diameter; ODR, ONSD-to-eyeball transverse diameter ratio; ETD, eyeball transverse diameter; CRA, central retinal artery. *Optic nerve diameter was available in 36 of 41 patients (moderate n=16, profound n=20).

S-20

Association Between Multiparametric Liver Ultrasonography Findings and Coronary Computed Tomography-Derived Liver Fat Measurements

Atiye Cenay Karabörk Kılıç[1], Pınar Baysan Şentürk[1], Selin Kart[1], Burcu Küçük Biçer[2], Sevcihan Kesen Özbek[1], Mahi Nur Cerit[1], Halit Nahit Şendur[1], Hüseyin Koray Kılıç[1], Gonca Erbaş[1], Suna Özhan Oktar[1]

[1] Department of Radiology, Gazi University Faculty of Medicine, Ankara, Turkey.

[2] Department of Medical Education and Informatics, Faculty of Medicine, Gazi University Faculty of Medicine, Ankara, Turkey

OBJECTIVE

To evaluate the associations between multiparametric liver ultrasonography parameters and computed tomography derived liver fat measurements in patients undergoing coronary artery calcium scoring and to explore their relationships with the presence of coronary artery calcification.

METHODS

This prospective study included 70 adults, 40 men and 30 women, with a mean age of 53.4 ± 9.2 years. They underwent non-contrast computed tomography for coronary artery calcium scoring between April and July 2024 and also underwent multiparametric liver ultrasonography. Hepatic attenuation was measured in Hounsfield units and converted to computed tomography derived proton density fat fraction (d-PDFF) using a previously published equation. Ultrasonographic parameters included ultrasound attenuation imaging (USAT), hepatorenal index (HRI), liver texture index (LTI), and liver stiffness measurement (LSM). Hepatic steatosis was operationally defined as d-PDFF >=5%. Associations were evaluated using Spearman rank correlation and the Mann-Whitney U test. Receiver operating characteristic curve analysis was performed, and paired areas under the curve were compared using the DeLong test.

RESULTS

USAT demonstrated the strongest correlation with d-PDFF (Spearman ρ=0.774, $p<0.001$), followed by HRI (ρ=0.659, $p<0.001$) and LTI (ρ=0.607, $p<0.001$). LSM was not significantly correlated with d-PDFF (ρ=0.150, $p=0.216$). USAT provided the highest discrimination for d-PDFF defined hepatic steatosis, with an area under the curve of 0.915 (95% confidence interval, 0.812-1.000), 78.0% sensitivity, and 90.9% specificity at a cut-off value of 0.60 dB/cm/MHz. The area under the curve for USAT was significantly higher than those for LTI (0.745, $p=0.006$) and HRI (0.719, $p<0.001$). Patients with a coronary artery calcium score greater than zero had higher d-PDFF values than patients without coronary calcification (median, 8.91% versus 6.01%, $p=0.037$).

CONCLUSION

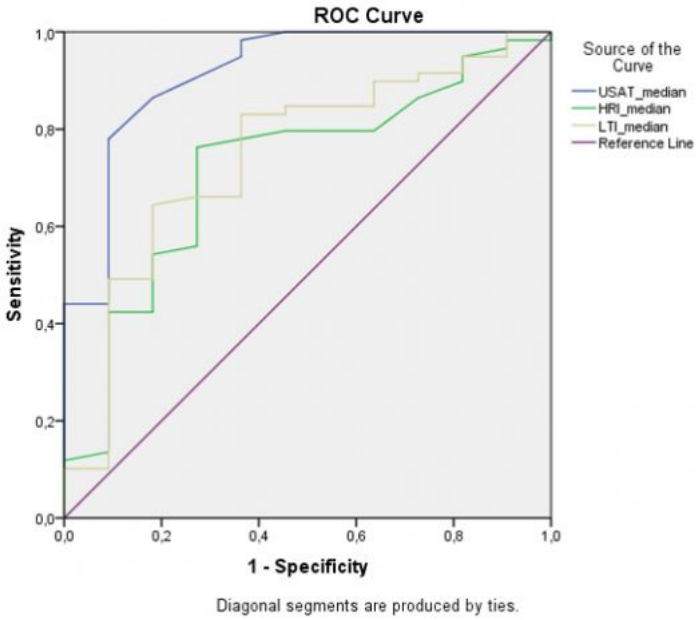
Among the evaluated multiparametric ultrasonography parameters, USAT showed the strongest association with computed tomography-derived liver fat. Higher computed tomography-derived liver fat was associated with the presence of coronary artery calcium.

KEYWORDS

hepatic steatosis, ultrasound attenuation imaging, multiparametric ultrasonography, computed tomography derived proton density fat fraction, coronary artery calcium

S-20 CONTINUED

Figure 1



Receiver operating characteristic (ROC) curves of multiparametric ultrasonography parameters for identifying d-PDFF-defined hepatic steatosis. USAT showed the highest diagnostic performance, followed by LTI and HRI. Hepatic steatosis was operationally defined as d-PDFF >=5%.

S-20 CONTINUED

Table 1. Participant characteristics (n=70)

Variable	Value
Age, years	53.4 ± 9.2
Male sex	40 (57.1)
BMI, kg/m²	28.8 ± 4.5
d-PDFF, %	6.88 (5.14-14.71)
Hepatic attenuation, HU	54.0 (40.5-57.0)
USAT, dB/cm/MHz	0.620 (0.590-0.710)
HRI	1.18 (1.05-1.40)
LTI	2.22 (1.63-2.56)
LSM, kPa	7.1 ± 1.3
CACS	0.0 (0.0-26.5)
Diabetes mellitus	20 (28.6)
Hypertension	28 (40.0)
Current smoking	33 (47.1)
Hyperlipidemia	30 (42.9)
History of coronary artery disease	5 (7.1)
Alcohol use	9 (12.9)
Other chronic disease	25 (35.7)

Data are presented as mean ± standard deviation, median (interquartile range), or n (%), as appropriate.

Table 2. Diagnostic performance for d-PDFF-defined hepatic steatosis

Parameter	AUC (95% CI)	Cut-off	Sensitivity, %
USAT	0.915 (0.812-1.000)	0.60	78.0
LTI	0.745 (0.578-0.912)	1.63	83.1
HRI	0.719 (0.552-0.886)	1.07	76.3

Parameter	Specificity, %	DeLong p vs USAT
USAT	90.9	*
LTI	63.6	0.006
HRI	72.7	<0.001

Hepatic steatosis was operationally defined as d-PDFF >=5%. Cut-offs maximize the Youden index.
*Paired AUCs were compared using the DeLong test, with USAT used as the comparator.

S-21

Diagnostic Utility of Quantitative Portal Doppler Parameters and Their Correlation With the FIB-4 Index in the Assessment of Portal Hypertension

Fatma Nur Bilgin[1], Ozdes Mahmutoglu[2], Abdullah Soydan Mahmutoglu[1]

[1] Department of Radiology, University of Health Sciences, Istanbul Training and Research Hospital, Istanbul, Türkiye

[2] Department of Radiology, University of Health Sciences, Şişli Hamidiye Etfal Training and Research Hospital, Istanbul, Türkiye

BACKGROUND AND AIMS

Non-invasive evaluation of portal hypertension and advanced hepatic fibrosis remains a critical challenge in the management of chronic liver disease.This study aims to investigate the diagnostic performance of quantitative portal vein Doppler parameters and their correlation with the non-invasive FIB-4 index

METHODS

A retrospective,single-center study was conducted on 115 consecutive patients who underwent abdominal color and spectral Doppler ultrasonography between January 1,2026, and June 30,2026.To eliminate inter-observer variability and technical bias,all examinations were performed on a single high-end ultrasound system,with portal and splenic measurements strictly acquired from reproducible, fixed anatomical landmarks.Portal vein diameter,peak systolic velocity,time-averaged maximum velocity,and portal congestion index(PCI) were calculated.Laboratory parameters obtained within a maximal 3-day window of the sonographic examination were utilized to compute the FIB-4 index.Statistical analyses included the Kolmogorov-Smirnov test for normality, Mann-Whitney U test,Spearman's rank correlation, and receiver operating characteristic (ROC) curve analysis(statistical significance defined as $p < 0.05$).

RESULTS

The study cohort comprised 115 patients(mean age,54.2 ± 11.8 years;64 males,51 females).Spearman correlation analysis revealed robust positive correlations between the FIB-4 index and both portal vein diameter and PCI($r=0.72, p<0.001$).Conversely,portal vein velocity demonstrated a statistically significant inverse correlation($r =-0.68$, $p<0.001$),decreasing from 18.4± 3.2 cm/s to 11.2 ± 2.5 cm/s in advanced stages.This velocity attenuation is consistent with the expected progressive hemodynamic deceleration secondary to increased intrahepatic resistance.The combined evaluation of portal Doppler parameters and the FIB-4 index yielded an area under the curve(AUC) of 0.91(95% CI:0.86-0.95) for predicting significant portal hemodynamic alterations.

CONCLUSIONS

The integration of quantitative portal Doppler parameters with the FIB-4 index provides a highly reliable, synergistic, and standardized non-invasive framework for stratifying portal hypertension severity in clinical practice.

KEYWORDS

Portal hypertension, doppler ultrasonography, FIB-4 index, portal ven, liver fibrosis

S-22

Carotid Hemodynamics and Local Arterial Stiffness in Systemic Sclerosis

Atiye Cenay Karabörk Kılıç[1], Ibrahim Vasi[2], Ece Altay[1], Semih Güllüoğlu[1], Ibrahim Karaduman[2], Burcu Küçük Biçer[3], Mahi Nur Cerit[1], Halit Nahit Şendur[1], Suna Özhan Oktar[1], Abdulsamet Erden[2]

[1] Department of Radiology, Gazi University Faculty of Medicine, Ankara, Turkey.

[2] Division of Rheumatology, Department of Internal Medicine, Gazi University Faculty of Medicine, Turkey.

[3] Department of Medical Education and Informatics, Faculty of Medicine, Gazi University Faculty of Medicine, Ankara, Turkey

AIM

Systemic sclerosis (SSc) is characterized by prominent microvascular vasculopathy, whereas the extent of macrovascular involvement remains uncertain. This study aimed to evaluate carotid arterial structure, hemodynamics, and local arterial stiffness in patients with SSc using advanced ultrasound-based vascular assessment.

METHODS

Participants were enrolled between November 2024 and June 2025. Forty-four patients with SSc and 34 healthy controls underwent carotid ultrasonography using a Mindray Resona R9 system. Vector Flow Imaging (VFI) was used to assess carotid hemodynamics, including maximum and mean systolic wall shear stress (WSS), turbulence-related parameters (TUR and TAT), and oscillatory shear index (OSI). Radiofrequency-based Vessel Quantitative Stiffness (RVQS) analysis was used to evaluate local arterial mechanical properties, including hardness coefficient (HC), pulse wave velocity (PWV), mean arterial diameter, and arterial distension. Carotid intima-media thickness (IMT) was also measured. Approximately normally distributed variables were compared using Welch's t-test and skewed variables using the Mann-Whitney U test; age-adjusted analyses were additionally performed.

RESULTS

Mean age was 55.1 ± 13.4 years in the SSc group and 50.4 ± 8.5 years in controls (p=0.063). IMT was similar between groups (0.724 ± 0.143 vs 0.718 ± 0.127 mm; age-adjusted p=0.571). No significant age-adjusted differences were observed for maximum WSS (p=0.152), mean systolic WSS (p=0.346), TUR (p=0.765), TAT (p=0.260), HC (p=0.798), PWV (p=0.726), mean arterial diameter (p=0.352), or distension (p=0.509). OSI was higher in SSc in the unadjusted analysis (p=0.018), but this difference did not remain significant after age adjustment (p=0.078) or multiple-testing correction (q=0.107).

CONCLUSION

No detectable differences in carotid structure, VFI-derived hemodynamics, or RVQS-derived local arterial stiffness were demonstrated between patients with SSc and healthy controls. These findings suggest that overt carotid macrovascular alterations may not be detectable in all SSc populations and may support the predominantly microvascular nature of SSc vasculopathy.

KEYWORDS

Systemic sclerosis, carotid artery, vector flow imaging, wall shear stress, radiofrequency-based vessel quantitative stiffness

S-22 CONTINUED

Table 1. Demographic characteristics and IMT classification

Characteristic	SSc (n=44)	Healthy controls (n=34)	p value
Age, years	55.1 ± 13.4	50.4 ± 8.5[a]	0.063
Female sex, n/N (%)	42/44 (95.5%)	32/34 (94.1%)	1.000
Normal IMT (<1.0 mm), n/N (%)	40/44 (90.9%)	33/34 (97.1%)	-

Values are presented as mean ± standard deviation or n/N (%). [a]Age data were available for 32 healthy controls. Age was compared using Welch's t-test and sex using Fisher's exact test. IMT was defined as the mean of three measurements.

Table 2. Comparison of carotid structural, hemodynamic, and local stiffness parameters

Parameter	SSc (n=44)	Healthy controls (n=34)	Unadjusted p	Age-adjusted p
IMT, mm	0.724 ± 0.143	0.718 ± 0.127	0.868	0.571
Maximum WSS, Pa	4.27 ± 1.23	3.96 ± 1.14	0.257	0.152
Mean systolic WSS, Pa	1.59 (1.15-2.24)	1.45 (1.28-1.95)	0.762	0.346
TUR	0.057 (0.033-0.123)	0.067 (0.033-0.143)	0.474	0.765
TAT	0.182 (0.070-0.403)	0.105 (0.048-0.256)	0.147	0.260
OSI	0.0067 (0-0.0211)	0 (0-0.0049)	0.018	0.078
HC	3.10 (2.44-4.18)	3.04 (2.24-3.66)	0.936	0.798
PWV, m/s	6.06 ± 1.70	5.77 ± 1.23	0.381	0.726
Mean diameter, µm	6925 ± 1034	6541 ± 933	0.089	0.352
Distension, µm	385.5 (318.8-500.2)	392.0 (355.0-534.8)	0.309	0.509

Normally distributed variables were compared using Welch's t-test and skewed variables using the Mann-Whitney U test. Age-adjusted analyses used HC3 robust OLS or rank-transformed ANCOVA, as appropriate. Adjusted analyses included 76 participants. The unadjusted OSI difference (p=0.018) was not significant after age adjustment (p=0.078) or Benjamini-Hochberg correction (q=0.107).

Poster Presentations

P-01

Ultrasound Diagnosis of Right Ovarian Torsion Associated With a Simple Ovarian Cyst: Correlation With Surgical Findings

Ayşenur Malkoç
Duzce University

AIM

To present the ultrasonographic findings of right ovarian torsion associated with a simple ovarian cyst in a young woman and to emphasize the importance of early diagnosis in preventing ovarian loss.

METHODS

A 21-year-old woman presented to the emergency department with severe lower abdominal pain persisting for two days. Pelvic ultrasound, Doppler ultrasonography, and contrast-enhanced computed tomography (CT) were performed. Imaging findings and surgical outcomes were retrospectively evaluated.

RESULTS

Ultrasound examination demonstrated a markedly enlarged right ovary associated with a simple ovarian cyst. Doppler ultrasonography findings documented absent vascular flow within the ovary, strongly suggesting ovarian torsion. Contrast-enhanced CT additionally demonstrated a markedly enlarged edematous right ovary with adnexal edema. Due to persistent severe pain and imaging findings, emergency surgery was performed. Intraoperatively, the right ovary was found to be twisted three times around its vascular pedicle. Despite detorsion attempts, ovarian perfusion could not be restored, and right oophorectomy was required because of irreversible ischemic damage.

CONCLUSION

Ovarian torsion should be considered in young women presenting with acute pelvic pain and an enlarged avascular ovary on ultrasound, particularly in the presence of an ovarian cyst. Combined grayscale and Doppler ultrasonography remains the primary imaging modality for rapid diagnosis and surgical decision-making. Delayed diagnosis may lead to irreversible ischemic injury and ovarian loss.

KEYWORDS

Ovarian torsion, Ultrasonography, Simple ovarian cyst, Surgical findings

P-01 CONTINUED

Figure 1



Figure 1.Grayscale ultrasonography demonstrating marked enlargement of the right ovary(short arrow) associated with a simple ovarian cyst (arrowhead). The left ovary is indicated by the long arrow.

Figure 2



Figure 2.Contrast-enhanced CT showing enlarged edematous right ovary (arrow) compatible with ovarian torsion.

P-02

Incidentally Diagnosed Takayasu Arteritis: A Case Report

Abdullah Gökçe, Irem Şen

SBU Gulhane Research and Training Hospital Department of Radiology,Ankara-Turkiye

INTRODUCTION AND OBJECTIVE

Takayasu arteritis (TA) is a chronic, large-vessel vasculitis primarily affecting the aorta and its main branches (1,2). Although most prevalent in young Asian females, it occurs across diverse demographics (3,4). Due to non-specific initial symptoms, diagnosis is frequently delayed until advanced vascular complications emerge (5). This case report underscores the clinical significance of imaging modalities in the incidental detection of TA.

CASE PRESENTATION

A 35-year-old female presented to the Otorhinolaryngology clinic with a one-month history of right anterior neck pain and was referred for cervical ultrasonography (US) under a preliminary diagnosis of lymphadenitis. US revealed diffuse wall thickening of the bilateral common carotid arteries (CCA), which was more pronounced on the right (Figures 1-3). Detailed anamnesis revealed a 9-year history of treated Crohn's disease, alongside mild, intermittent lightheadedness and exertional upper-extremity fatigue.

Suspecting TA, computed tomography angiography (CTA) of the head and neck was performed, demonstrating circumferential wall thickening and luminal narrowing of the thoracic aorta and supra-aortic branches (Figures 4,5). Based on correlative clinical, laboratory, and imaging findings, the Rheumatology department diagnosed the patient with TA. Medical therapy was initiated, and the patient was taken into follow-up.

DISCUSSION AND CONCLUSION

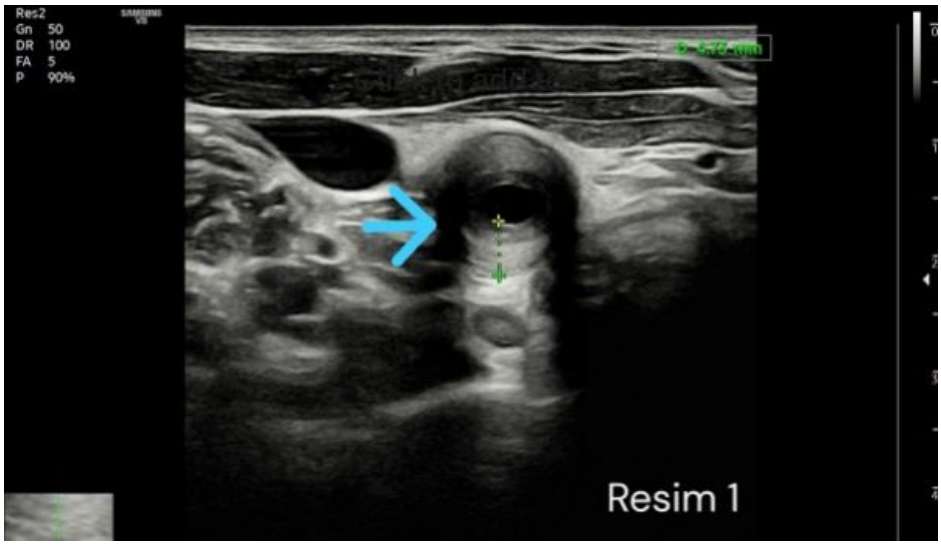
Since its initial description by Mikito Takayasu in 1905, TA remains a rare vasculitis predominantly affecting Asian populations (1,5). Its exact pathophysiology is not yet fully elucidated (6). The insidious onset of symptoms often delays diagnosis (7). In conclusion, as illustrated by this case, vascular manifestations of TA can be incidentally identified via cervical ultrasonography in patients presenting with non-specific symptoms, enabling accurate diagnosis through subsequent advanced imaging.

KEYWORDS

Takayasu Arteritis, Large Vessel Vasculitis, Ultrasonography, Computed Tomography Angiography, Common Carotid Artery

P-02 CONTINUED

Figure 1



Diffuse wall thickening and luminal narrowing of the right common carotid artery

Figure 2



Diffuse wall thickening and luminal narrowing of the right common carotid artery

P-04

Incidental Triorchidism in a 22-Year-Old Man: Sonographic Findings

Mertcan Avcı, Barış Turk

Department of Radiology, University of Health Sciences Türkiye, Şişli Hamidiye Etfal Training and Research Hospital, Istanbul, Türkiye

AIM

Polyorchidism is a rare congenital anomaly characterized by the presence of more than two testes. Most cases are asymptomatic and are detected incidentally. We present a case of triorchidism diagnosed on scrotal ultrasonography in a 22-year-old man who had no scrotal complaints.

METHODS

A 22-year-old man was referred from the urology clinic for scrotal color Doppler ultrasonography during evaluation for dysuria. The examination was performed with a 6-11 MHz linear transducer. Testicular location, size, echotexture and focal lesions were assessed, together with the epididymides, tunica vaginalis and pampiniform plexus.

RESULTS

The right and left testes were normally located in the scrotum and measured 50 × 24 mm and 43 × 21 mm, respectively. A third testicular structure was seen in the left hemiscrotum, immediately adjacent to the upper pole of the left testis. It measured 21 × 18 × 14 mm, with an estimated volume of 2.8 mL. Its echogenicity and homogeneous parenchymal appearance were the same as those of the orthotopic testes. No solid or cystic focal lesion was identified in any of the three testes. Both epididymides were normal, and there was no hydrocele. The right pampiniform plexus was mildly prominent, measuring 2.6 mm, without reflux. The overall findings were consistent with intrascrotal triorchidism.

CONCLUSION

Although rare, polyorchidism should be kept in mind when an additional scrotal structure has the same sonographic appearance as normal testicular tissue. Ultrasonography allows confident diagnosis in typical cases and can also demonstrate associated scrotal abnormalities, helping to avoid unnecessary intervention.

KEYWORDS

polyorchidism, triorchidism, scrotal ultrasonography

P-05

"Cold" Nodule Hides in a "Hot" Thyroid: Papillary Thyroid Carcinoma With Tall Cell Cytomorphology in Graves' Disease

Muhammed Ibrahim Erbay[1], Ozcan Hurmuzlu[1], Ahmet Samil Karadag[1], Muhammet Fatih Cakmak[2], Ibrahim Adaletli[1]

[1] Department of Radiology, Istanbul Cerrahpasa University Hospital, Istanbul, Turkiye

[2] Department of Otorhinolaryngology, Istanbul Cerrahpasa University Hospital, Istanbul, Turkiye

INTRODUCTION

Although thyroid carcinoma arising in hyperfunctioning glands is uncommon, hyperthyroidism may lead to underestimation of the malignant potential of a focal hypoechoic nodule. Tall cell variant papillary thyroid carcinoma (TCV-PTC) is among the most aggressive differentiated subtypes.

CASE PRESENTATION

A 48-year-old male, previously operated for colon carcinoma with no family history, was documented hyperthyroid in 2022. Graves' disease was diagnosed on biochemical hyperthyroidism, TRAb positivity, and diffusely increased tracer uptake on scintigraphy, which also showed a nodule at the right lobe-isthmus junction with lower uptake than surrounding parenchyma. No sonographic risk stratification or cytology followed.

Antithyroid medication initially normalized thyrotropin and thyroid hormone concentrations. Three years later, TRAb rose to 14.9 U/mL (reference <1.5), with return to biochemical hyperthyroidism (TSH <0.005 µIU/mL, free T3 9.31 pg/mL, free T4 2.98 ng/dL). Palpable nodularity prompted sonography, revealing a heterogeneous, hypervascular gland of normal volume containing a 30×17 mm hypoechoic solid nodule with coarse calcifications and extrathyroidal extension (ACR TI-RADS 5) (Figures 1&2). Bilateral cervical nodes showed hilar effacement, marked vascularity, and heterogeneous hypoechoic areas (Figures 2&3). Ultrasound-guided aspiration of the isthmic nodule yielded papillary carcinoma with tall cell cytomorphology. Positron emission tomography confirmed intense uptake in the primary lesion and cervicomediastinal nodes, without distant metastasis (Figure 5). Total thyroidectomy with neck dissection was scheduled.

DISCUSSION

TCV-PTC comprises 5-10% of papillary carcinomas and is defined by oncocytic cells at least twice as tall as wide. It is associated with higher-stage disease, increased extrathyroidal extension, nodal metastasis, recurrence, and reduced radioiodine avidity compared with conventional papillary carcinoma. Here, the index nodule showed lower tracer uptake than surrounding hyperfunctioning parenchyma three years before diagnosis, yet was not subsequently characterised.

CONCLUSION

Diffuse thyroid hyperfunction should not provide reassurance regarding focal nodules with discordant tracer uptake. Such nodules warrant sonographic risk stratification and cytology when indicated.

KEYWORDS

Ultrasonography, Tall-cell Variant Papillary Thyroid Carcinoma, Hypofunctioning Nodule, Hyperthyroidism, Thyroid scintigraphy

P-05 CONTINUED

PET

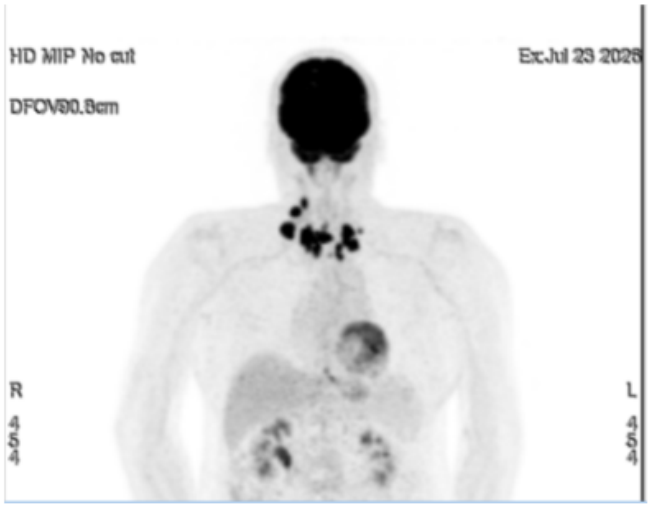


Figure 2: Positron emission tomography (PET) result showing intense uptake within the primary thyroid lesion and cervicomediastinal nodes, without distant metastasis.

Figure 2: Positron emission tomography (PET) result showing intense uptake within the primary thyroid lesion and cervicomediastinal nodes, without distant metastasis.

Sonographic Images

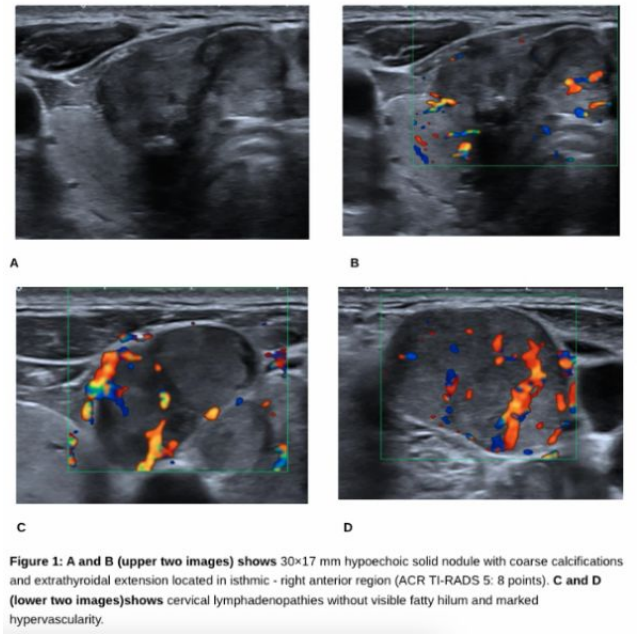


Figure 1: A and B (upper two images) shows 30×17 mm hypoechoic solid nodule with coarse calcifications and extrathyroidal extension located in isthmic - right anterior region (ACR TI-RADS 5: 8 points). **C and D (lower two images)shows** cervical lymphadenopathies without visible fatty hilum and marked hypervascularity.

Figure 1: A and B (upper two images) shows 30×17 mm hypoechoic solid nodule with coarse calcifications and extrathyroidal extension located in isthmic - right anterior region (ACR TI-RADS 5: 8 points). C and D (lower two images)shows cervical lymphadenopathies without visible fatty hilum and marked hypervascularity.

P-06

Beyond the Weigert-Meyer Rule: Sonographic Findings of Ureterocele in an Incomplete Duplex Collecting System

Ege Furkan Narbay, Deniz Can Demirci, Mert Akaltın, Alper Özel

Department of Radiology, University of Health Sciences, Şişli Hamidiye Etfal Training and Research Hospital, Istanbul, Türkiye

BACKGROUND

Duplex collecting system is one of the most common congenital anomalies of the urinary tract and may be either complete or incomplete. In complete duplication, the relationship between the two ureters is classically described by the Weigert-Meyer rule: the ureter draining the upper renal moiety inserts more inferomedially and is therefore prone to obstruction and ureterocele formation, whereas the lower moiety is more commonly associated with vesicoureteral reflux. In incomplete duplication, the two ureters join before reaching the bladder and share a common distal course. Consequently, the classic Weigert-Meyer relationship does not directly explain the complications encountered in these patients. Altered peristalsis and uretero-ureteral, or “yo-yo” reflux at the point of fusion have been described and may contribute to asymmetric collecting-system dilatation.

CASE PRESENTATION

A 73-year-old woman with diabetes mellitus underwent renal ultrasonography during evaluation for renal end-organ involvement. Ultrasonography demonstrated an incomplete duplex collecting system of the left kidney. The upper moiety showed mild pelvicalyceal dilatation, and the renal parenchyma was diffusely echogenic. Two ureteral limbs were traced to their fusion within the proximal third, continuing distally as a single ureter. An approximately 1-cm intravesical ureterocele was identified at the posteroinferior aspect of the urinary bladder.

DISCUSSION

Preferential upper-moiety dilatation despite a common distal ureter may reflect altered urinary dynamics. Distal outflow resistance related to the ureterocele, asynchronous ureteral peristalsis, and uretero-ureteral reflux are possible contributing mechanisms. Yo-yo reflux was not dynamically demonstrated in this patient and therefore remains a possible rather than confirmed explanation.

CONCLUSION

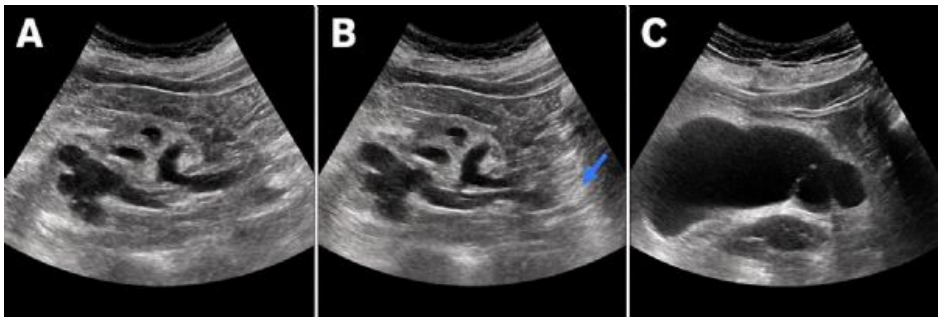
Ultrasonography can delineate the renal moieties, demonstrate the level of ureteral fusion, and identify an associated ureterocele in a single examination. Recognizing incomplete duplication is important because its anatomy and functional consequences cannot be interpreted solely according to the classic Weigert-Meyer rule.

KEYWORDS

Duplex collecting system, incomplete ureteral duplication, ultrasonography, ureterocele, yo-yo reflux

P-06 CONTINUED

Figure 1



A. Longitudinal renal ultrasound demonstrates upper and lower moieties separated by an intervening parenchymal band, with drainage into two distinct renal pelves. The upper moiety is mildly more dilated than the lower moiety. The renal parenchyma shows diffuse increased echogenicity, consistent with parenchymal renal disease. B. Ultrasound demonstrates two distinct ureters coursing separately. On sonographic tracing of the ureters, fusion was observed at the level indicated by the blue arrow, within the proximal third of their course, after which they continued distally as a single ureter. C. Transverse bladder ultrasound demonstrates an approximately 1-cm thin-walled ureterocele at the left ureterovesical junction.

P-07

When Trauma Changes the Story: Ultrasound Reveals a Superficial Dermatofibrosarcoma Protuberans Masquerading as a Post-Traumatic Collection

E. Banu Kayan[1], Halil Karataş[1], Erdem Özkan[2], Mehtap Balaban[1]

[1] Department of Radiology, Ankara Bilkent City Hospital, Ankara, Turkey

[2] Department of Radiology, Kastamonu Training and Research Hospital, Kastamonu, Turkey

AIM

To demonstrate how systematic ultrasound reassessment redirected the diagnostic pathway in a superficial soft-tissue mass presenting with post-traumatic collection-like features.

METHODS

The clinical course and imaging findings of an 18-year-old man with an ankle mass were evaluated with ultrasound, radiography, and MRI, with correlation to ultrasound-guided core biopsy, histopathology, and surgical findings.

RESULTS

Initially, the patient presented with left ankle swelling following a fall. Ultrasound demonstrated an echogenic subcutaneous abnormality with oedema and weak peripheral vascularity, reported as inflammatory change.

Two years later, following blunt re-trauma, he returned with swelling, erythema and difficulty weight-bearing. Radiography showed soft-tissue swelling without osseous abnormality. Clinically, haematoma with abscess was suspected. During acute evaluation, the lesion was interpreted as a poorly circumscribed, heterogeneous, complex collection-like lesion on sonography. Aspiration was attempted but yielded no material, prompting repeat sonographic examination. This demonstrated an irregularly marginated, heterogeneous, non-compressible, semisolid lesion involving the dermis and subcutaneous tissue, without displaceable fluid, but with internal arterial flow, inflammatory changes and associated superficial thrombophlebitis. Strain elastography was heterogeneous and non-contributory. Sonographic impression favoured an inflamed mesenchymal soft-tissue mass. MRI demonstrated a heterogeneously enhancing subcutaneous mass and defined its local extent, although vascular malformation was considered. Ultrasound-guided core biopsy and wide excision confirmed dermatofibrosarcoma protuberans (DFSP). Follow-up imaging showed no recurrence or distant disease.

CONCLUSION

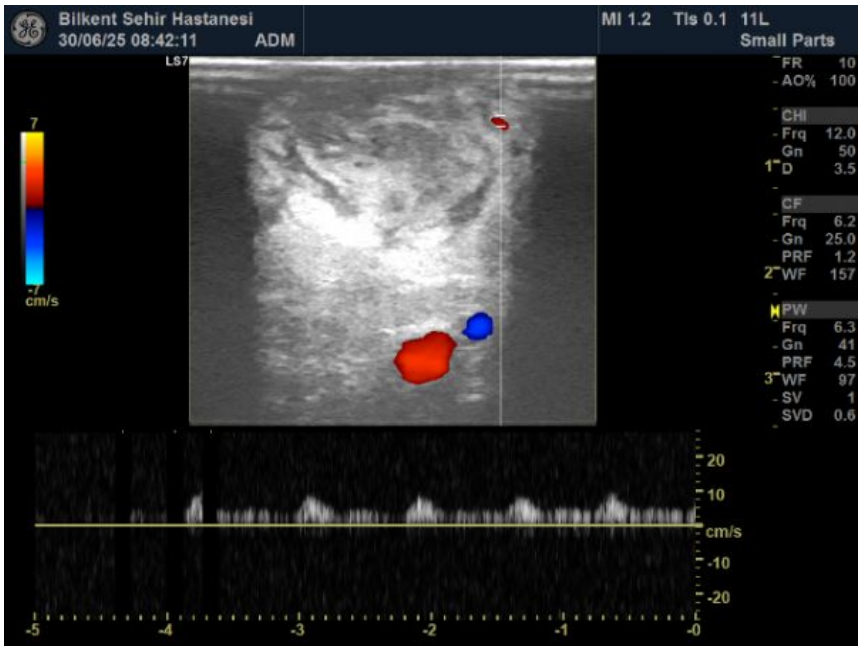
DFSP has been reported in trauma-related presentations and can mimic a post-traumatic haematoma.[1,2] In this case, trauma complicated the presentation of a pre-existing tumour and promoted anchoring on an acute collection. Clinical history should inform, but not anchor, imaging interpretation, emphasising systematic assessment of lesion composition, compressibility, fluid mobility, Doppler vascularity, and prior imaging.[3] MRI defined local extent but remained indeterminate. Nonproductive aspiration with discordant sonographic findings should prompt reassessment of lesion composition and consideration of tissue diagnosis.

KEYWORDS

Dermatofibrosarcoma protuberans, Ultrasonography, Post-traumatic collection, Superficial soft-tissue mass, Diagnostic pitfall

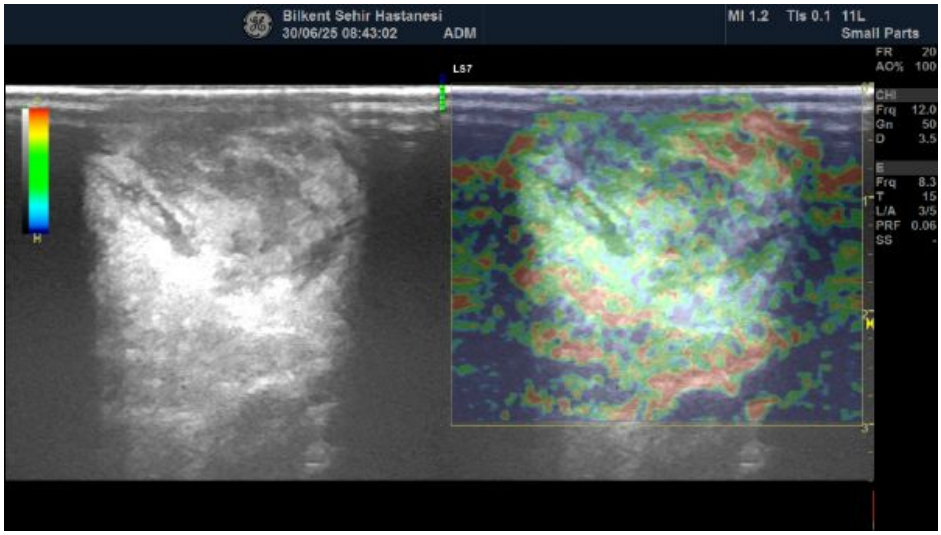
P-07 CONTINUED

Figure1a



Superficial, heterogeneous, irregularly marginated soft-tissue mass with internal arterial vascularity on color and spectral Doppler, despite its collection-like appearance in the setting of trauma. The presence of internal flow and absence of displaceable fluid on dynamic assessment supported a solid lesion rather than a haematoma or abscess.

Figure1b



Qualitative strain elastography of the same lesion demonstrates heterogeneous stiffness, with variation in stiffness corresponding to the heterogeneous internal architecture on grayscale imaging.

P-08

Look Beyond the Intussusception: Ultrasound Detection of a Juvenile Pedunculated Polyp

Öznur Altan, Derya Bako

Department of Radiology, Ondokuz Mayıs University Faculty of Medicine, Samsun, Türkiye

AIM

Juvenile polyps are common benign colorectal lesions in children and may serve as pathological lead points for intussusception (1). Ultrasound is the primary imaging modality for pediatric intussusception and enables real-time assessment during and after non-surgical reduction. We aimed to raise awareness of juvenile polyps as potential pathological lead points in pediatric intussusception and emphasize the importance of careful sonographic evaluation after successful reduction.

METHODS

We present a 3-year-old female patient with clinical and sonographic findings of intussusception who underwent successful hydrostatic reduction. Following complete reduction, a control abdominal ultrasound examination was performed. The bowel was systematically evaluated for residual intussusception and potential underlying intraluminal lesions. The detected lesion was assessed for its location, size, echogenicity, internal architecture, relationship with the bowel wall, presence of a pedicle, and vascularity on color Doppler imaging.

RESULTS

A 9 × 11 mm pedunculated intraluminal polypoid lesion was detected at the hepatic flexure on post-reduction ultrasound. The lesion was hypoechoic and homogeneous, with a hyperechoic peripheral rim and small internal anechoic spaces. A vascular pedicle connecting the lesion to the bowel wall was demonstrated, with prominent vascularity on color Doppler examination (Figure 1). These sonographic findings were highly suggestive of a juvenile polyp. Following polypectomy, histopathological examination confirmed the diagnosis.

CONCLUSION

Although most pediatric intussusception cases are idiopathic and are thought to be related to transient hypertrophy of lymphoid tissue (2), pathological lead points should not be overlooked. Juvenile polyps, although less common, may serve as lead points and can be detected by ultrasound after successful reduction. Therefore, systematic post-reduction sonographic evaluation of the bowel is essential to identify an underlying pathological lead point and potentially prevent recurrent intussusception.

REFERENCES

1. Vitale V, et al. J Ultrasound. 2014;19:53-55.

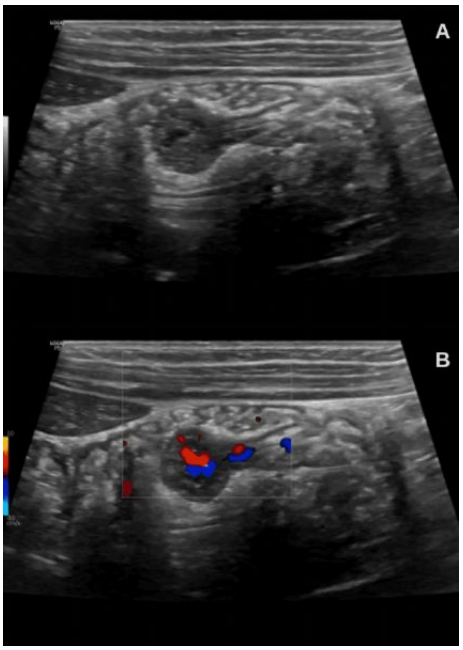
2. Long B, et al. Am J Emerg Med. 2025;91:37-45.

KEYWORDS

Polyp, Intussusception, Ultrasound

P-08 CONTINUED

Figure 1



Post-reduction ultrasound demonstrates a 9 × 11 mm pedunculated hypoechoic polyp at the hepatic flexure, with an echogenic rim and small anechoic foci (A). A vascular stalk with prominent color Doppler flow is seen (B).

P-09

What Hides Behind Bilateral Hydroureteronephrosis? Pelvic Organ Prolapse Missed on Ultrasonography

Tuba Pınar Abay, Gökhan Polat, Enes Yılmaz

Department of Radiology, Kütahya Health Sciences University, Kütahya, Türkiye

PURPOSE

Advanced pelvic organ prolapse (POP) is a rarely considered but reversible cause of obstructive uropathy: a prolapsed uterus can kink or compress the ureters, causing bilateral hydroureteronephrosis. The diagnosis is easily missed on ultrasound - a bladder emptied by uterine pressure becomes invisible, and the prolapsed uterus can mimic a pelvic mass. Clinical history: A 78-year-old woman with stage 4 CKD (baseline creatinine 1.5-2.0 mg/dL) and a history of sacrocolpopexy presented with acute-on-chronic kidney injury.

MATERIAL-METHODS

Renal ultrasound: Grade 3-4 bilateral pelvicalyceal dilatation (AP diameter 24/25 mm); obstruction confirmed, cause unknown. Pelvic ultrasound: The bladder was not visualised - emptied and compressed by the prolapsed uterus. A 5.99 × 4.67 cm hypoechoic mass occupied the bladder fossa, indistinguishable from a bladder tumour or extrinsic pelvic mass; CT was performed. CT: Grade 4 uterine prolapse with bilateral ureteral kinking confirmed the obstruction. Treatment: Bilateral percutaneous nephrostomy yielded 800 mL in 24 hours. Follow-up ultrasound showed bilateral regression to grade 1; creatinine returned to baseline (1.8 mg/dL).

RESULT

Nephrostomy relieved the obstruction - hydroureteronephrosis regressed from grade 3-4 to grade 1 and creatinine normalised. The pelvic structure was unchanged, confirming the anatomical cause persisted.

CONCLUSION

Advanced POP can cause severe obstructive uropathy and be missed on ultrasound. An empty bladder or unexplained pelvic mass on pelvic ultrasonography in an elderly woman with bilateral hydroureteronephrosis should prompt suspicion for prolapse; CT should not be delayed. Nephrostomy is an effective bridge, but definitive urogynaecological management remains essential - obstruction relief does not correct the prolapse.

TEACHING POINTS

Ultrasound detects hydronephrosis early but is unreliable in the pelvis: a prolapsed uterus can empty the bladder and mimic a pelvic mass. In elderly women with unexplained bilateral hydroureteronephrosis and rising creatinine, pelvic organ prolapse must be included in the differential diagnosis.

KEYWORDS

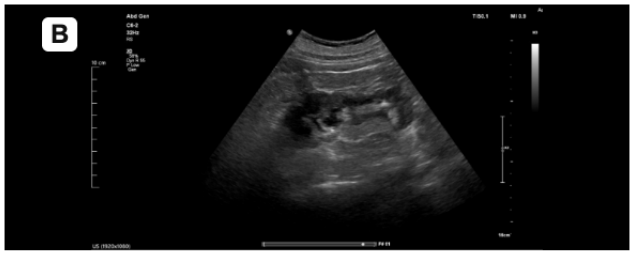
♀, Pelvic Organ Prolapse, Hydroureteronephrosis, Obstructive Uropathy

P-09 CONTINUED

Figure 1.



13 AUGUST 2026 BEFORE URINARY DECOMPRESSION
Renal US - severe pelvicalyceal dilatation



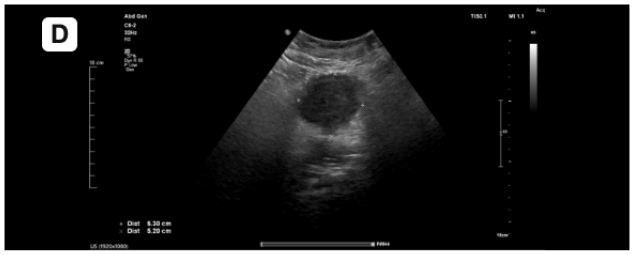
28 AUGUST 2026 AFTER BILATERAL PERCUTANEOUS NEPHROSTOMY (14 AUGUST)
Renal US - collecting system decompressed

(A) Renal ultrasound - severe bilateral pelvicalyceal dilatation, thinned parenchyma. (B) Post-nephrostomy renal ultrasound - bilateral regression to grade 1.

Figure 2.



13 AUGUST 2026 BEFORE URINARY DECOMPRESSION
Pelvic US - 5.99 × 4.67 cm, central anechoic component



28 AUGUST 2026 AFTER BILATERAL PERCUTANEOUS NEPHROSTOMY (14 AUGUST)
Pelvic US - 5.30 × 5.20 cm, structure persists

(C) Pelvic ultrasound - 5.99 × 4.67 cm mass in the bladder fossa; prolapsed uterus has emptied the bladder, which is not visible.(D) Pelvic structure persists at 5.30 × 5.20 cm; prolapse anatomically unchanged.